Earth and Planetary Science Letters 441 (2016) 10–25

Contents lists available at ScienceDirect

Earth and Planetary Science Letters

www.elsevier.com/locate/epsl

Astronomical tuning of the end-Permian extinction and the Early Triassic Epoch of South China and Germany

Mingsong Li [a,b], James Ogg [a,c], Yang Zhang [a,c], Chunju Huang [a,*], Linda Hinnov [b,d], Zhong-Qiang Chen [a], Zhuoyan Zou [a]

[a] State Key Laboratory of Biogeology and Environmental Geology, School of Earth Sciences, China University of Geosciences, Wuhan 430074, Hubei, PR China
[b] Department of Earth and Planetary Sciences, Johns Hopkins University, Baltimore, MD 21218, USA
[c] Department of Earth, Atmospheric and Planetary Sciences, Purdue University, 550 Stadium Mall Drive, West Lafayette, IN 47907-2051, USA
[d] Department of Atmospheric, Oceanic, and Earth Sciences, George Mason University, Fairfax, VA 22030, USA

ARTICLE INFO

Article history:
Received 24 July 2015
Received in revised form 6 December 2015
Accepted 6 February 2016
Editor: M. Frank

Keywords:
Triassic time scale
cyclostratigraphy
magnetostratigraphy
mass extinction
recovery
end-Permian

ABSTRACT

The timing of the end-Permian mass extinction and subsequent prolonged recovery during the Early Triassic Epoch can be established from astronomically controlled climate cycles recorded in continuous marine sedimentary sections. Astronomical-cycle tuning of spectral gamma-ray logs from biostratigraphically-constrained cyclic stratigraphy through marine sections at Meishan, Chaohu, Daxiakou and Guandao in South China yields an integrated time scale for the Early Triassic, which is consistent with scaling of magnetostratigraphy from climatic cycles in continental deposits of the Germanic Basin. The main marine mass extinction interval at Meishan is constrained to less than 40% of a 100-kyr (kilo-year) cycle (i.e., <40 kyr) and the sharp negative excursion in $\delta^{13}C$ is estimated to have lasted <6 kyr. The sharp positive shift in $\delta^{13}C$ from −2‰ to 4‰ across the Smithian–Spathian boundary at Chaohu was completed in 50 kyr. The earliest marine reptiles in the Mesozoic at Chaohu that are considered to represent a significant recovery of marine ecosystems did not appear until 4.7 myr (million years) after the end-Permian extinction. The durations of the Griesbachian, Dienerian, Smithian and Spathian substages, including the uncertainty in placement of widely used conodont biostratigraphic datums for their boundaries, are 1.4 ± 0.1, 0.6 ± 0.1, 1.7 ± 0.1 and 1.4 ± 0.1 myr, implying a total span for the Early Triassic of 5.1 ± 0.1 myr. Therefore, relative to an assigned 251.902 ± 0.024 Ma for the Permian–Triassic boundary from the Meishan GSSP, the ages for these substage boundaries are 250.5 ± 0.1 Ma for base Dienerian, 249.9 ± 0.1 Ma for base Smithian (base of Olenekian stage), 248.2 ± 0.1 Ma for base Spathian, and 246.8 ± 0.1 Ma for the base of the Anisian Stage. This astronomical-calibrated timescale provides rates for the recurrent carbon isotope excursions and for trends in sedimentation accumulation through the Early Triassic of studied sections in South China.

1. Introduction

Life was nearly annihilated during the end-Permian mass extinction (EPME) 252 million years ago (Ma). A prolonged and unstable biotic recovery through the Early Triassic was punctuated by recurrent anomalously hot climate episodes, carbon-cycle perturbations and global ocean anoxia (e.g., Burgess et al., 2014; Chen and Benton, 2012; Payne et al., 2004; Sun et al., 2012; Wignall, 2015). The causes, timing and rates of the EPME and these repeated environmental disruptions have yet to be explained, partly because age models for the Early Triassic are highly disputed (Burgess et al., 2014; Galfetti et al., 2007; Ogg, 2012; Szurlies, 2007; Wu et al., 2012).

A reliable chronology is the requirement for calibrating the rates of these dramatic Early Triassic events. Radio-isotopic dating of Late Permian–Early Triassic had produced contradictory ages for the same events due to application of different methods or standards by different laboratories (e.g., Bowring et al., 1998; Burgess et al., 2014; Mundil et al., 2004; Shen et al., 2011). The revised EARTHTIME tracer solutions (e.g., Burgess et al., 2014) do not

* Corresponding author.
E-mail addresses: mli69@jhu.edu (M. Li), jogg@purdue.edu (J. Ogg), zhan2214@purdue.edu (Y. Zhang), huangcj@cug.edu.cn (C. Huang), lhinnov@gmu.edu (L. Hinnov), zhong.qiang.chen@cug.edu.cn (Z.-Q. Chen), zouzhyqd@gmail.com (Z. Zou).

http://dx.doi.org/10.1016/j.epsl.2016.02.017
0012-821X/

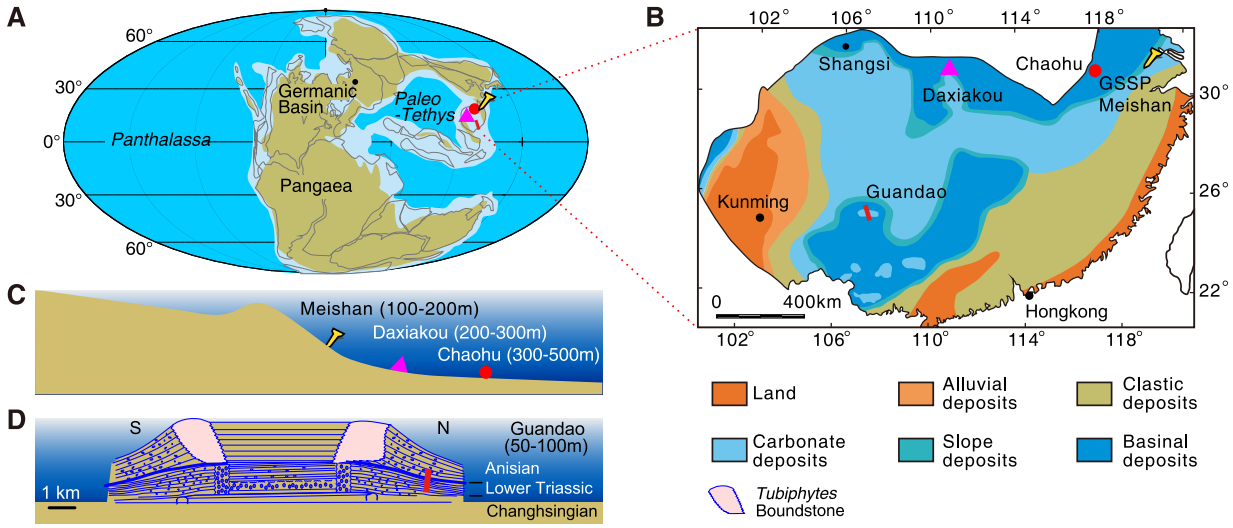

Fig. 1. Paleogeography maps. **A**. Early Triassic global paleogeographic map (modified from http://www.scotese.com). **B**. Early Triassic paleography of South China (modified from Feng et al., 1997). **C**. Sketch of paleo-depths of the studied Meishan, Chaohu and Daxiakou sections (Song et al., 2013a). **D**. Schematic cross section of the depositional setting for the Changhsingian to Anisian strata of the Great Bank of Guizhou in the Nanpanjiang Basin of South China (Lehrmann et al., 1998) with paleo-depth of Guandao section according to Song et al. (2013a).

allow a linear transformation of dates from previously measured zircons; therefore, estimating the Early Triassic stages/substages durations by combination/comparison of published zircon dates cannot be undertaken until zircons from those volcanic ash layers are remeasured using the new tracers and protocols. Another complication is that some zircon populations appear to be clustered at ages that are older than the volcanic ash bed or yield artifacts of younger ages due to lead-loss that can not be entirely removed by standard laboratory methods. An excellent example of such complications is the apparently non-sequential U–Pb dates derived from several volcanic ash beds that bracket the Olenekian/Anisian stage boundary at the Monggan/Wantou section in South China (Ovtcharova et al., 2015).

The Milankovitch concept is that quasi-periodic oscillations in the Earth's tilt and its orbit around the Sun induce prominent 10^4–10^6 yr variations in the Earth's seasonal contrasts, and that these climatic oscillations are recorded in the stratigraphic record (e.g., Hays et al., 1976; Hinnov, 2013). When combined with other stratigraphic methods, such as biostratigraphy, magnetostratigraphy and radio-isotopic dating, the analysis and interpretation of astronomically-modulated climatic signals derived from proxies in sedimentary rocks yield a high-resolution astronomical time scale (ATS) (Hinnov and Hilgen, 2012). However, compiling a reliable ATS requires (1) high-resolution climate proxy records from continuous successions, (2) confirmation that detected sedimentation cycles have an origin from astronomical-climate cycles, and (3) verified assignment of detected cycles to specified astronomical parameters. Efforts to apply cyclostratigraphy method to the Early Triassic epoch have yielded conflicting interpretations, partly because recognized sedimentation wavelengths were assigned to an astronomical parameter (precession, obliquity, eccentricity) based mainly on their presumed consistency with selected radio-isotopic dates. For example, the duration of the Griesbachian substage using interpreted short-eccentricity (~100 kyr) tuning is ca. 1.3 myr in Germany (Kozur and Weems, 2011), but only 0.73 myr at the West Pingdingshan section (Guo et al., 2008) and a brief 0.49 myr at the Daxiakou section (Wu et al., 2012).

We applied cyclostratigraphic analysis to spectral gamma-ray logs of multiple Permian–Triassic conodont-zoned marine sections on the South China carbonate platform to compile an integrated 5.1-myr-long ATS for the entire Early Triassic Epoch. The magnetostratigraphy of this cycle-tuned composite from South China correlates well to the independent studies of cycle-tuned magnetostratigraphy from continental successions in the Germanic basin (Kozur and Bachmann, 2008; Menning and Käding, 2014; Szurlies, 2004, 2007). This inter-regional ATS provides a high-resolution integrated time scale for the end-Permian through Early Triassic record of climate change and evolution.

2. Materials and methods

2.1. Yangtze Platform sections

During the Early Triassic, the South China Plate was located at the eastern part of the Paleo-Tethys Ocean and isolated from the Pangaea supercontinent (Fig. 1). The well-preserved Upper Permian through Lower Triassic marine successions have been extensively studied. Three sections from the northern margin of the Yangtze Platform and one section from the Great Bank of Guizhou in the northern portion of the Nanpanjiang Basin were used to establish the Early Triassic timescale.

The Meishan section in Zhejiang Province contains the Global Boundary Stratotype Section and Point (GSSP) for the Permian–Triassic boundary (PTB) (Yin et al., 2001), and the Chaohu section is a candidate for the GSSP of the Induan–Olenekian boundary of the Lower Triassic (Tong et al., 2003). The Guandao section on the northern margin of the Great Bank of Guizhou is a significant section for the Olenekian–Anisian boundary (OAB) because it contains both the proposed conodont markers and magnetic-reversal marker, and it has dated volcanic ash beds that bracket for the OAB (Lehrmann et al., 2006, 2015).

The GSSP for the PTB (base of Griesbachian substage) is defined at the first appearance datum (FAD) of conodont *Hindeodus parvus* at Meishan (Yin et al., 2001), and this FAD is also recorded at Daxiakou (Zhao et al., 2013). The base of the Dienerian has been placed at the base of the conodont *Sweetospathodus kummeli* Zone at Chaohu (Zhao et al., 2007) and Daxiakou (Zhao et al., 2013). The proposed GSSP candidate level at Chaohu for the base-Olenekian is at the FAD of the conodont *Novispathodus waageni eowaageni*, which is immediately below the base of the ammonoid *Flemingites–Euflemingites* Zone (Tong et al., 2003). The Smithian–Spathian substage boundary in these sections is assigned to the base of the conodont *Novispathodus pingdingshanensis* Zone, which is accompanied by a sharp positive shift in $\delta^{13}C$ that serves as a

global marker (Tong et al., 2007). The OAB is assigned as the FAD of conodont *Chiosella timorensis* at Guandao (Lehrmann et al., 2006, 2015). It should be emphasized that, other than the base-Triassic GSSP that defines the base of the Griesbachian Stage, there is not yet an international agreement on the definition of the boundaries of the Lower Triassic substages.

The Chaohu and Daxiakou sections are dominated by quasi-even-bedded bundles of carbonate and claystone from the lower Griesbachian through middle Spathian. The Daxiakou section has thinner limestone and mudstone beds compared to Chaohu. The Lower Guandao section is extremely weathered; therefore, we logged a new fresh road-cut Guandao 3 (or Mingtang) section that is 300 m south of the Lower Guandao section. Detailed information on the lithology, biostratigraphy and carbon isotope stratigraphy of each section is in the Supplementary Information.

2.2. Spectral gamma-ray logs of the sections

Total gamma-ray intensity (GR) of sediments is dominated by potassium (K), uranium (U) and thorium (Th) contents due to their abundance and half-lives (e.g., Ruffell and Worden, 2000; Schnyder et al., 2006). K is common in many minerals such as clays, feldspar, mica, and chloride salts. U and Th are concentrated in a number of sedimentary host minerals including clays, feldspar, heavy minerals, and phosphate, and U is often concentrated in organic matter (Schnyder et al., 2006). Nevertheless, delayed recovery after the EPME questions organic matter as a key contribution of variations in GR and U in the Early Triassic. Therefore, high GR values are typically attributed to clay-rich sediments, whilst lower GR values are generally linked with coarser-grained rocks and carbonates. However, a high proportion of volcanic ash is accompanied by elevated levels of Th and K, but not in U; and these artifacts of volcanic-related peaks in GR within the Meishan and Guandao sections were removed prior to spectral analysis (e.g., Appendix Fig. A.5).

One cause of variable clay content can be orbital-climate signals, such as the situation during high eccentricity when hotter summers relative to winters would have resulted in an intensified weathering and monsoonal climate. More rainfall and runoff would result in more clay into marine environment and hence high GR and U, and vice versa. Another factor can be variations in average sea level that will affect relative influxes of carbonate and clay fractions. Therefore, spectral GR log is appropriate for use in paleoclimatic research, sequence stratigraphy and analysis of orbital-forced sedimentary cycles.

GR was measured using a RS-230 BGO Super-SPEC gamma detector with K, U and Th channels. The instrument has a detection area of approximately 20-cm diameter. This results in a smoothing effect in GR cross the section to reduce high frequency signals (most are non-Milankovitch band climate signals and noise) and enhance low frequency signals that mainly are Milankovitch band signals. Our measurements with a recording time of 60–120 s were at 5 to 20 cm intervals depending on rock types: 5-cm intervals at Meishan and the lower 40 m of the Daxiakou section, 10-cm intervals in the upper Daxiakou section and the lower and upper Chaohu sections, from 5 to 20 cm intervals at the middle Chaohu section, and 20-cm intervals at Guandao section.

2.3. Time-series methods

Detection and interpretation of high-frequency cyclicity in the GR records requires several steps:

(1) To remove long-term trends, the GR series were pre-whitened in *Kaleidagraph* software by subtracting 15% to 35% weighted averages (Cleveland, 1979).

(2) For an initial survey of stratigraphic frequencies and trends of the untuned and tuned GR series, plus detection of changing accumulation rates, a sliding-window spectral analysis was performed using evolutive Fast Fourier transform (FFT) spectrograms with *evofft.m* (Kodama and Hinnov, 2014).

(3) Based on the indicated wavelengths of major cyclicity and visual examination for potential 405-kyr or 100-kyr oscillations, Gaussian bandpass filtering was applied in *Analyseries 2.0.8* (Paillard et al., 1996) to aid in the isolation of potential astronomical parameters.

(4) The GR series were tuned to an interpreted astronomical cycle ("minimum tuned" with linearly interpolation) (Hinnov, 2013), and then resampled in *Analyseries* (Paillard et al., 1996) based on those identified potential 405-kyr (or 100-kyr) cycles.

(5) The power spectra of the tuned records were examined for higher-frequency peaks that correspond to predicted orbital solution for Early Triassic (Laskar et al., 2004). Both the untuned and tuned data were analyzed with the multi-taper method (MTM) spectral estimator (Thomson, 1982); estimated spectra were tested against robust red noise models at the 90%, 95% and 99% confidence levels (Mann and Lees, 1996).

(6) The interpretations and tuned model were adjusted to incorporate additional stratigraphic and magnetostratratigraphic information on potential hiatuses, relative accumulation rates, and hypothesized magnetic polarity correlations. Steps 3–6 are an iterative process until the evolutive spectra of the cycle-tuned stratigraphy models show stable positions and continuity of multiple orbital-cycle bands throughout each section.

(7) The high-resolution floating ATS is anchored to a high-precision radioisotope date to complete the calibration to numerical time.

2.4. Magnetostratigraphy of Chaohu sections

The Induan succession at Chaohu was densely sampled for magnetostratigraphy by Sun et al. (2009). We re-examined the original sample-by-sample demagnetization data (provided by Zuming Sun) to separate the high-quality, medium-quality and indeterminate results into a revised polarity column with the main clusters of polarity. We then extended this study upward by adding approximately 120 minicores through the slightly overturned and relatively limestone-rich uppermost Smithian through Spathian portions of the Chaohu composite section. The general magnetic characteristics upon thermal demagnetization for these new samples were similar to those reported by Sun et al. (2009) for the clay-rich Induan. To test the reproducibility of our interpretations, these new datasets were independently analyzed by Zhiming Sun, who gave nearly identical assignments of the polarity reliabilities and characteristic directions. See Supplementary Information for details of these paleomagnetic studies.

3. Results

Details of each interpreted long-eccentricity (E) cycle at these sections are given in Supplementary Information, and the general features are summarized below.

3.1. Meishan cyclostratigraphy

Even though the Meishan section is relatively compact in both meters and chronostratigraphy, the temporal span of the GR and U series are well-constrained by a set of high-precision U–Pb dates derived using revised EARTHTIME tracer solutions (Burgess et al., 2014). Guided by these constraints, we assigned 13 short-eccentricity (~100 kyr) cycles modulated by slightly more than 3 long-eccentricity cycles over 26 m of the GR and U series (Fig. 2A).

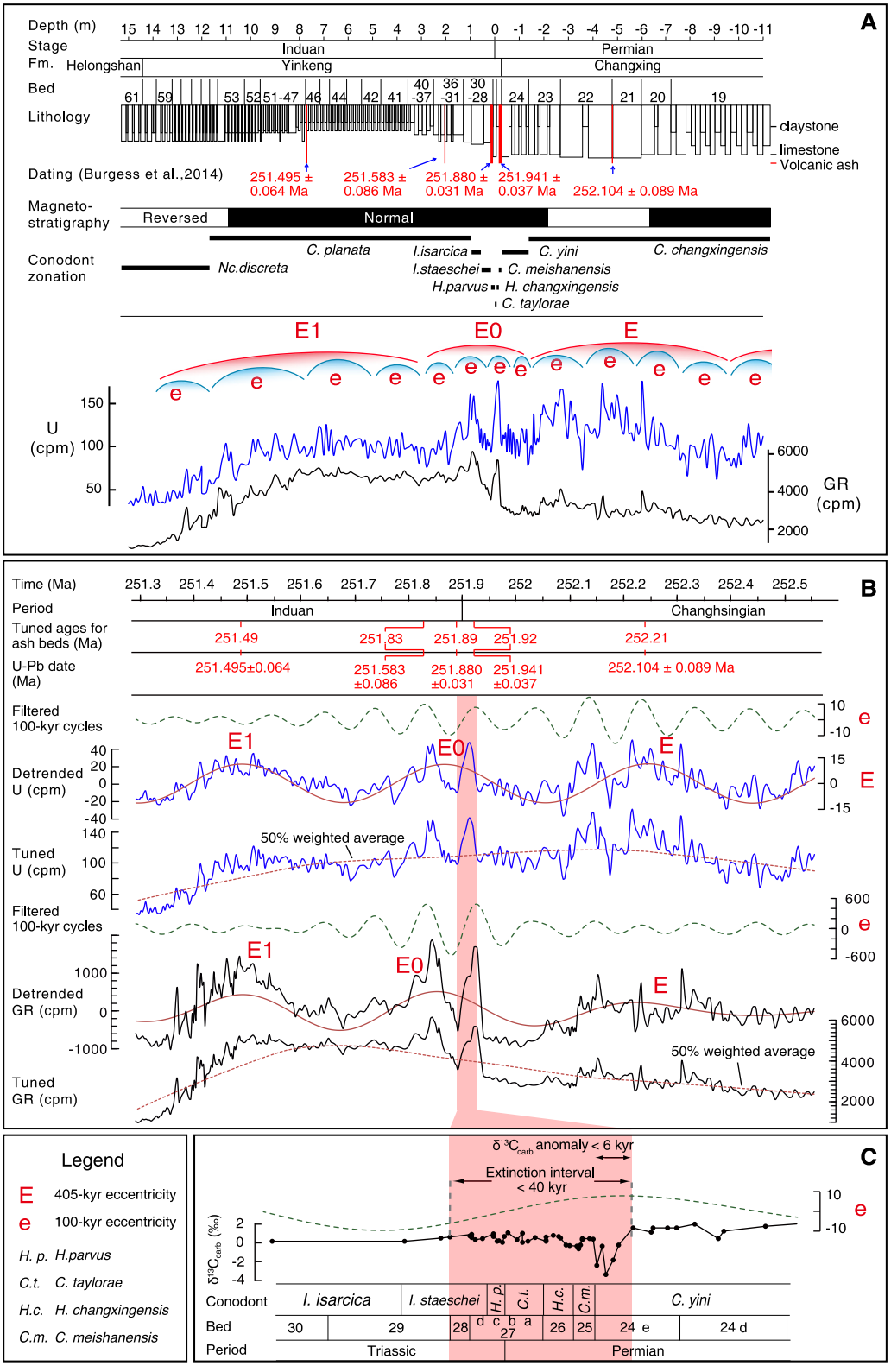

Fig. 2. Stratigraphy and interpreted cyclostratigraphy of the Meishan section. **A**. GR and U series are shown with initial assignment of eccentricity cycles constrained by high-precision radiometric dates from Burgess et al. (2014) (detailed in Appendix Fig. A.2); magnetic polarity zones are from Li and Wang (1989); and conodont zones are from Zhang et al. (2009). **B**. 100-kyr-tuned GR and U series after removing 50% weighted average with filtered 405-kyr and 100-kyr eccentricity cycles (Gauss filter, passband: 0.00248 ± 0.0005 and 0.01 ± 0.0025 cycles/kyr, respectively) showing U–Pb dates of ash beds (Burgess et al., 2014) and tuned ages for those ash beds. **C**. Mass extinction interval at Meishan in reddish shading with filtered 100-kyr cycles in B, bed numbers and conodont zones (Zhang et al., 2009) and with $\delta^{13}C$ data (Shen et al., 2011). Conodont zones: *C.m.* = *Clarkina meishanensis*, *H.c.* = *Hindeodus changxingensis*, *C.t.* = *C. taylorae*, *H p.* = *H parvus*, and *I.s.* = *Isarcicella staeschei*.

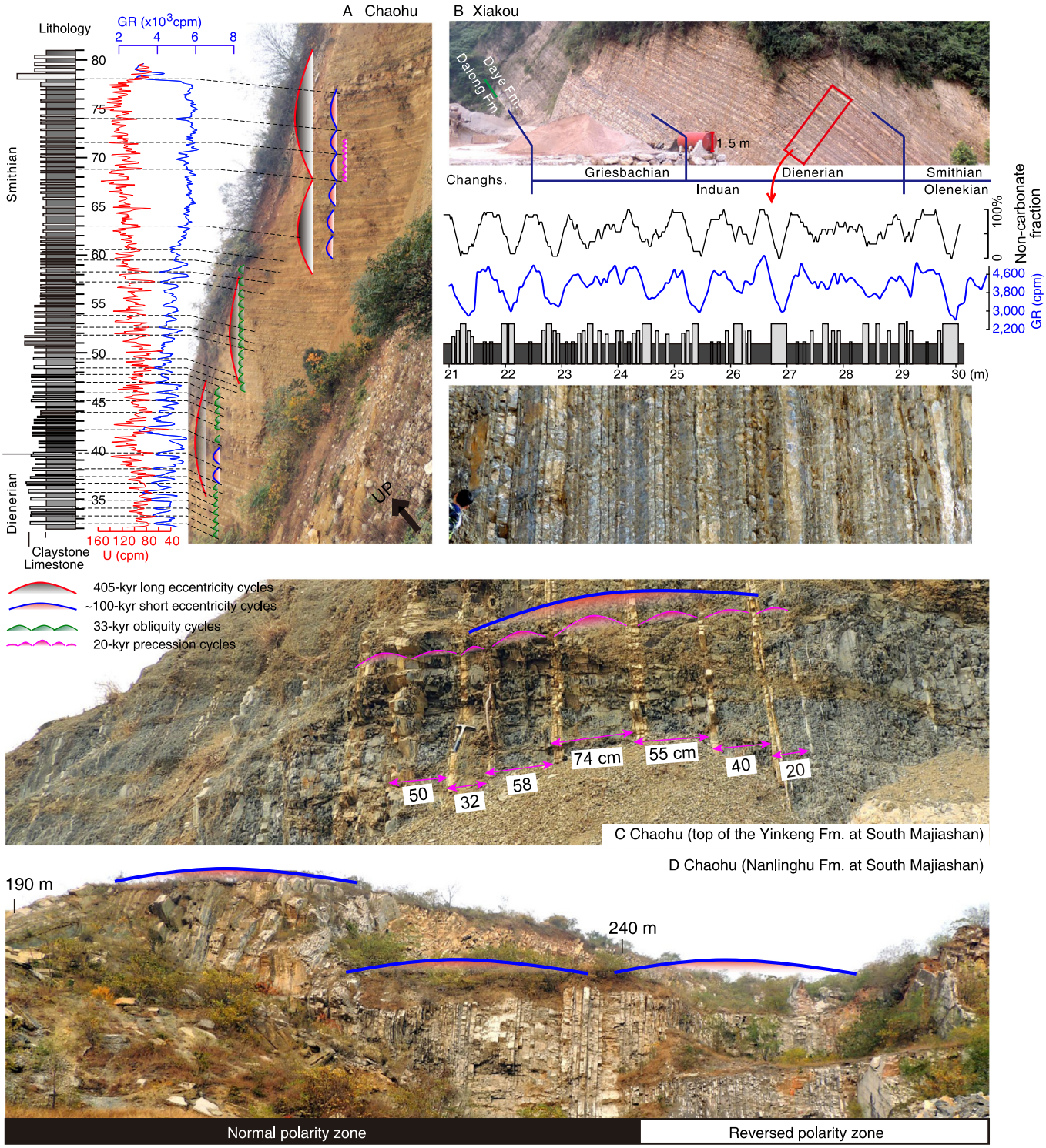

Fig. 3. Field photos and astronomical cycle interpretations of the Chaohu and Daxiakou sections. **A**. Chaohu's North Majiashan section of upper Dienerian and Smithian (with the photograph of the steeply dipping strata rotated to correspond to the stratigraphic column). GR (blue curve) and U (red curve) with interpreted astronomical cycles of precession (marked by the green line) grouped into short-eccentricity bundles (denoted as pink-filled arcs) that are modulated in long-eccentricity bundle-sets (denoted by grey-filled arcs). **B**. Daxiakou section. GR (blue curve) from 21 to 30.6 m compared to a 20-cm sliding window of the percentage of non-carbonate composition (black curve; where 0% indicates pure carbonate and 100% is pure clay). **C**. Section of middle Spathian at Chaohu with five interpreted precession-cycles that each culminate in a carbonate-rich interval (pink arcs; cycle thicknesses in cm) that have progressively increasing then decreasing influxes of clay as these precession cycles are modulated by a short-eccentricity cycle (blue arc, bundle-set spanning ca. 2.5 m). **D**. The upper Spathian of the Nanlinghu Formation at Chaohu is characterized by major lithologic cycles between thick-bedded limestone sets and intervals of thin-bedded carbonate with clayey interbeds. These 30-m-thick major cycles are interpreted as either 100-kyr short-eccentricity bundles in preferred Option #1 or as 405-kyr long-eccentricity modulations in Option #2. The magnetic polarity of this section is shown at bottom of diagram. (For interpretation of the references to color in this figure legend, the reader is referred to the web version of this article.)

Interpretations of eccentricity cycles in the Permian from the U and GR series are identical with those interpreted from magnetic susceptibility at Meishan by Wu et al. (2013). Because this series is too short to tune using 405-kyr cycles; therefore, we tuned the GR and U series to these 100-kyr cycles. Minimum tuning of GR and U data to this single orbital frequency can be used to assess the success or failure of the presumption in resolving other astronomical parameters. The spectrum of 100-kyr-tuned U series has additional significant peaks at 405 kyr, 25 kyr, and 20 kyr (Fig. 7), which are consistent with predicted Early Triassic astronomical terms for long-eccentricity, perhaps an obliquity component (but slightly shifted from the predicted 33-kyr frequency) and the 20-kyr precession (Laskar et al., 2004) (La2004 ETP in Fig. 7), and thus support our assigned tunings.

3.2. Chaohu and Daxiakou cyclostratigraphy

Lithological cycles are especially evident at the well-exposed Chaohu and Daxiakou sections. At both sections, the upper Induan and Smithian are characterized by quasi-evenly-spaced sets of carbonate–claystone cycles (Fig. 3A and 3B). And in the middle Smithian of uppermost Yinkeng Formation at Chaohu, the varying thicknesses and amplitude of these claystone- to carbonate-rich progressions are interpreted as sets of precession cycles modulated by a ca. 2.5-m-thick short-eccentricity cycle (Fig. 3C).

At Chaohu, the GR series of the lower Griesbachian–middle Smithian interval from 10 to 74 m is characterized by cyclic variations with wavelengths of ~10 m, ~2.3 m, 0.7–1.1 m and 0.5 m (Figs. 3 and 4). Comparison of the ratios of these cycle wavelengths with the ratios of Milankovitch frequencies implies that these cycles represent 405-kyr, ~100-kyr, 33-kyr, and 20-kyr cycles, respectively with a mean accumulation rate of 2.4 cm/kyr (24 m/myr).

The power spectra of the Daxiakou section displays a similar suite of peak ratios. The GR series of Griesbachian through lower Spathian (0–80 m interval) is characterized by 9 m, 2.5–3.5 m, 0.8–1.4 m, and 0.55 m wavelengths (thickness ranges are due to slight changes in mean accumulation rate), which fit the expected ratios of the 405-kyr, ~100-kyr, 33-kyr and 20-kyr cycles (Fig. 7).

The power spectra of these GR stratigraphic series vary smoothly throughout the Chaohu and Daxiakou sections. The average thicknesses of carbonate beds progressively increases from the uppermost Dienerian through middle Spathian at Chaohu (interval of 74 m through 184 m). Therefore, the cyclic variations become progressively broader with average wavelengths of ~34 m, 9 to 13 m, 3 to 4 m, and ~2 m (see Fig. 4; and Appendix Fig. A.4 and Fig. A.6 for lithological cycles in measured section). The ratios of these wavelengths suggest these cycles represent 405-kyr, ~100-kyr, 33-kyr and 20-kyr cycles, respectively, which indicate average sedimentation rate of ca. 8 cm/kyr (80 m/myr) during the middle Spathian is three times more than the rate during the Dienerian.

In the thick-bedded carbonates of upper Spathian at Chaohu from 184 m to 280 m, the GR series is characterized by cyclic variations with 30 m, 10 m and 4–6 m wavelengths (Fig. 4), which have 2 main alternative interpretations. Option #1 is that these three wavelengths represent ~100-kyr, 33-kyr and 20-kyr cycles. Option #2 is that 30 m wavelength is the same period (405-kyr) as the ~34-m main cycles in the underlying interval of 74–184 m (Fig. 5). Option #1 is supported by the progressive increasing accumulation rates as revealed in the evolutive FFT spectrum (Appendix Fig. A.7). These local increases in accumulation rates at the Chaohu and Daxiakou sections on the north margin of South China Plate are mainly an increased influx of carbonate. Option #2 would entail a total of more than 15.5

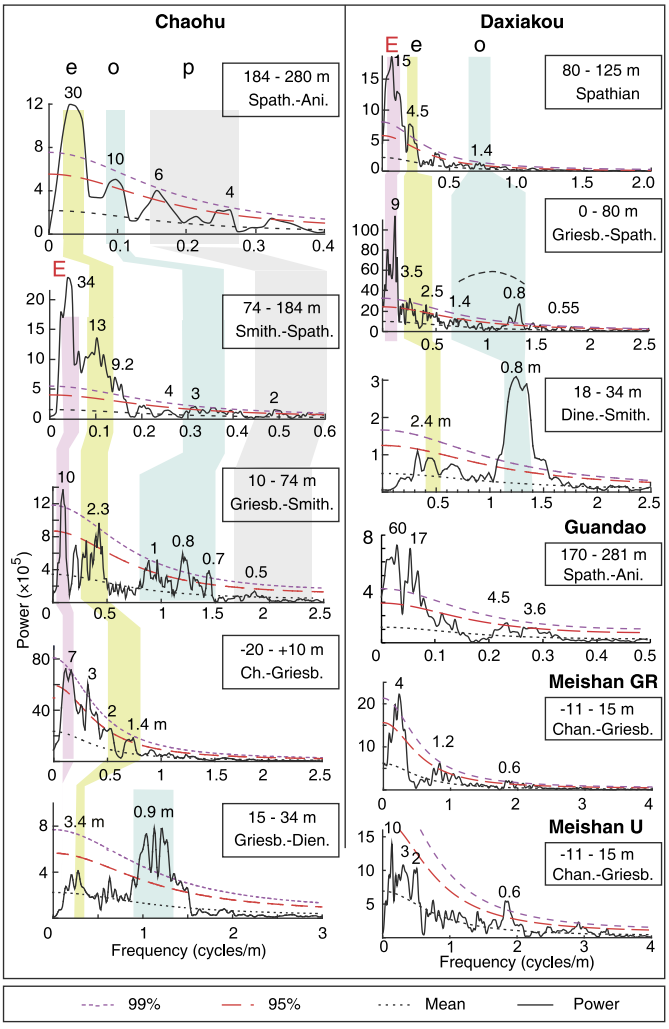

Fig. 4. Results of spectral analyses. 2π MTM power spectra of untuned GR series from intervals in the Chaohu, Guandao and Daxiakou sections that have relatively stable sediment accumulation rates. **Chaohu** intervals are 184–280 m (top panel), 74–184 m, 10–74 m, −20 to +10 m and 15–34 m (bottom panel), less a 50%, 35%, 25%, 35% and 35% weighted average, respectively. **Daxiakou** intervals from top to bottom are 80–125 m, 0–80 m, and 18–34 m less a 66%, 35%, and 50% weighted average trend, respectively. **Guandao** section interval is 170–281 m, less a 66% weighted average trend. **Meishan** section (−11 to +15 m) less a 35% weighted average for both GR and U (detailed in Appendix Fig. A.2). All spectra are shown with a robust red-noise model calculated with linear fitting and a 20% median smoothing window following the recommended settings in Mann and Lees (1996) Appendix A.

long-eccentricity cycles spanning the Early Triassic, therefore implying a duration longer than 6.3 myr. Therefore, this Option #2 would project the age of the Olenekian/Anisian boundary as ca. 245.6 Ma relative to a base-Triassic at 251.9 Ma (Burgess et al., 2014), which is significantly younger than published radio-isotopic dates that indicate an age of ~247 Ma (Lehrmann et al., 2015; Ovtcharova et al., 2015). To help resolve this uncertainty in both age and accumulation rates, we acquired magnetostratigraphy for the Spathian at Chaohu.

The distinctive magnetostratigraphy matched the main features of the reference polarity scale derived from Svalbard and Canadian Arctic (e.g., synthesis by Hounslow and Muttoni, 2010) and of the 100-kyr-scaled polarity pattern from the Germanic Basin (Szurlies, 2004, 2007) (Fig. 8 and Appendix Fig. C.5). The results show that (1) the OAB is at or within the onset of the Dongma'anshan Formation limestone breccia, and (2) the 30-m cycles in relative clay enrichment correspond to clay-sand oscillations interpreted as 100-kyr cycles in the Germanic Basin. Therefore,

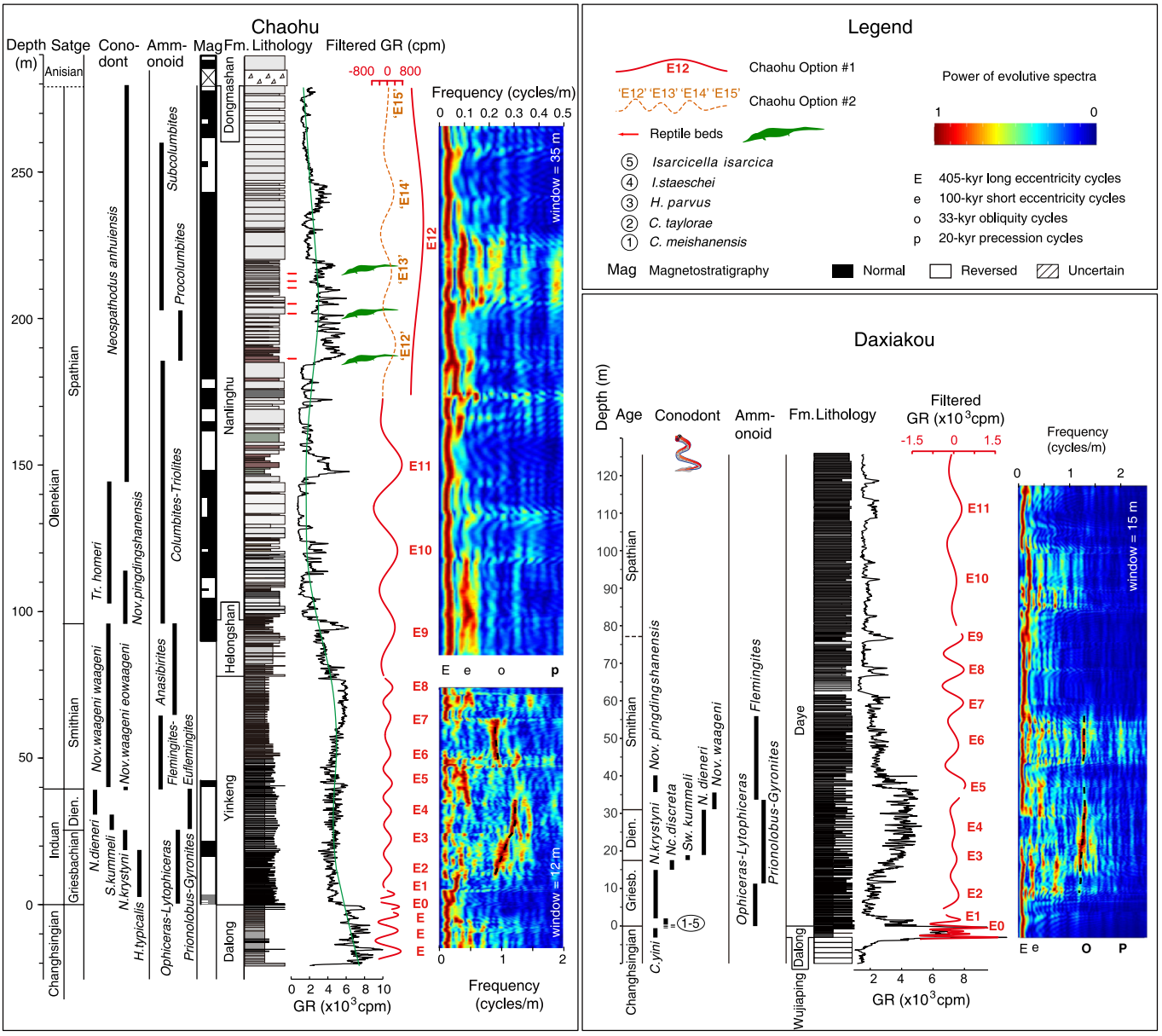

Fig. 5. Interpreted cyclostratigraphy of the Chaohu and Daxiakou sections, South China, in the depth (meters) domain. **Chaohu**: Conodont and ammonoid zones at Chaohu are from Zhao et al. (2007). See Appendix Fig. A.4 and Fig. A.6 for details. Magnetic polarity zones are from Sun et al. (2009) and this study. Half-bars are questionable polarity subzones represented by only a single sample. Chaohu GR series (black curve) with 35% weighted average trend (green curve). Chaohu evolutive FFT spectrum (colored area) uses 12-m and 35-m sliding window for −20 to 80 m and 74 to 279.6 m, respectively. Chaohu filtered cycles (red "E" curve from Gauss filter, passband: 0.14 ± 0.04, 0.20 ± 0.05, 0.1 ± 0.25 and 0.03 ± 0.015 cycles/m for −20 to −2 m, −2 to 5 m, 5 to 80 m and 80 to 280 m, respectively) are interpreted as 405-kyr cycles (detailed in Appendix B.1). Two interpretations for uppermost Spathian cycles in the interval from 174 to 280 m are shown as explained in the main text and Appendix Fig. A.7: in red (our preferred Option #1) this limestone-rich interval has a high accumulation rate with 100-kyr cycles under a single 405-kyr envelope, and in dashed brown (Option #2) these oscillations are four 405-kyr cycles with no change in accumulation rate. Reptile beds at Chaohu are indicated by silhouettes following Motani et al. (2015). **Daxiakou**: Conodont and ammonoid zones at Daxiakou are from Zhao et al. (2013). GR data are shown with its evolutive FFT spectrum using a 15 m sliding window and filtered cycles (red "E, Gauss filter, with passbands: 1.0 ± 0.4, 0.10 ± 0.07, 0.10 ± 0.04 and 0.05 ± 0.03 cycles/m for −3.5 to 1 m, 5 to 35 m, 38 to 78 m and 80–125 m respectively) which are interpreted as 405-kyr cycles. (For interpretation of the references to color in this figure legend, the reader is referred to the web version of this article.)

Chaohu Option #2 is possible only if both the cycle-tuned magnetostratigraphy of uppermost Spathian through basal Anisian in the Germanic Basin (Szurlies, 2004, 2007) and the radio-isotopic dating constraints for the base-Triassic (Burgess et al., 2014) and/or the base-Anisian (Lehrmann et al., 2015; Ovtcharova et al., 2015) have uncertainties more than 1 million-year. Therefore, we prefer Option #1, in which the 30-m-thick oscillations in the uppermost Spathian of Chaohu represent 100-kyr eccentricity cycles. However, in Appendix Fig. A.8, we also give the implications of Option #2, in which those 30-m wavelengths are assigned as 405-kyr long-eccentricity cycles.

3.3. Guandao cyclostratigraphy

The spectrum of the GR of Guandao from upper Spathian to lower Anisian (170–281 m) shows significant peaks at 60 m, 17 m, and 4.5 to 3.6 m (Fig. 4). The main features of this ca. 111 m GR pattern has three main alternative interpretations, depending on the assumptions of changing sediment accumulation rates (see extended discussions in Appendix Section A.4.3 and Fig. A.11). Option #1 is that the 17-m-thick cycles within the interval from 175 to ~240 m are 100-kyr cycles within a 405-kyr cycle of ca. 65-m wavelength; followed by a sudden slowing in accumu-

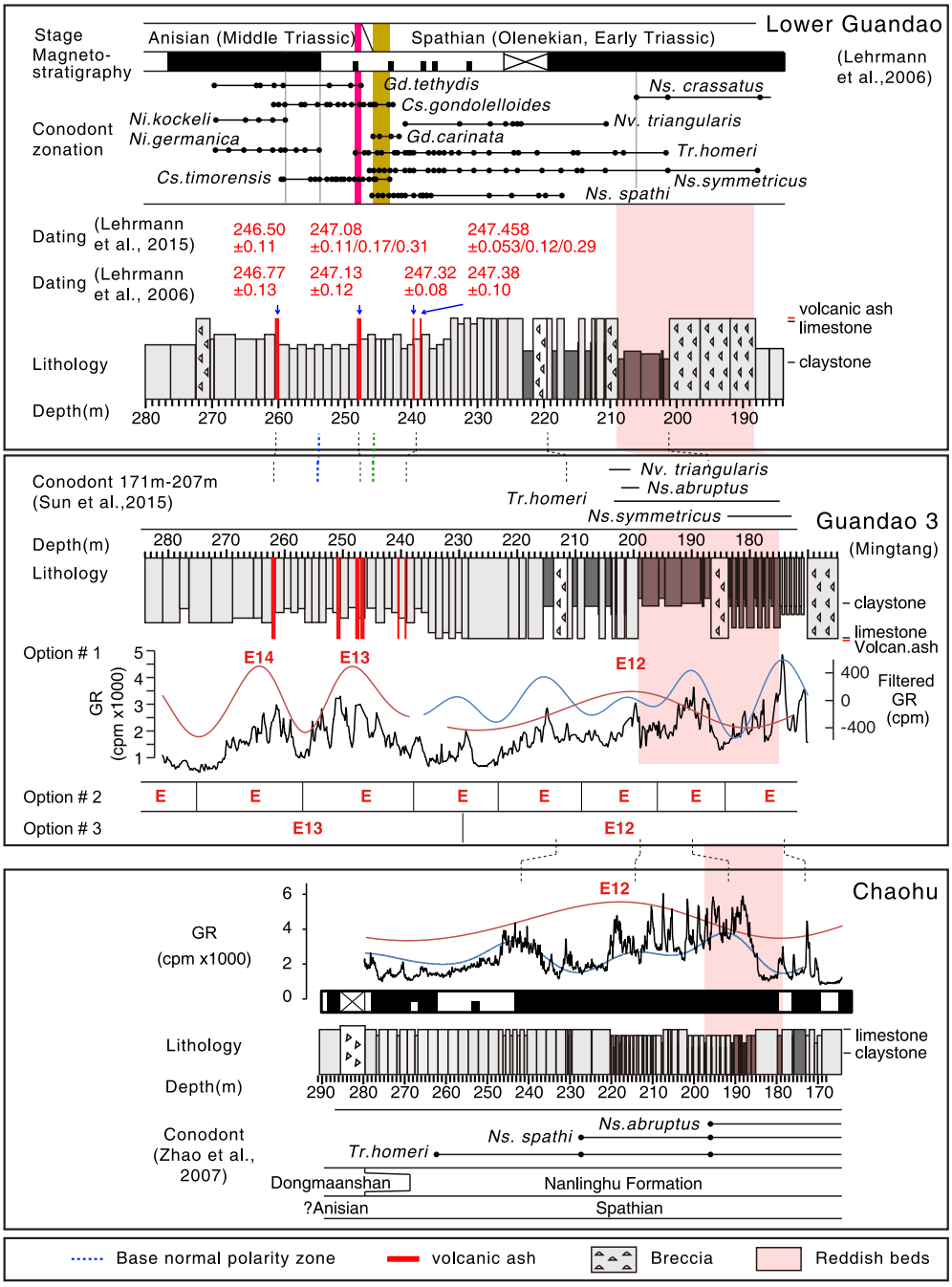

Fig. 6. Cyclostratigraphy interpretation of the Guandao sections and projection via magnetostratigraphy to Chaohu in upper Spathian and lowest Anisian. Pink shading denotes intervals that are dominated by reddish-colored facies in each section. **Lower Guandao**: Chrono-, magneto- and litho-stratigraphy and radiometric dating are from Lehrmann et al. (2006, 2015). The brown band shows residual maximal horizon of overlapping conodont ranges for *Gladigondolella carinata* and *Ch. timorensis* for the base of the Olenekian–Anisian transition (OAB interval) while the pink band indicates residual maximal horizon of overlapping *Gd. tethydis* and *Tr. homeri* for the top of the Olenekian–Anisian transition following the scheme of Goudemand et al. (2012). **Guandao 3 (Mingtang)**: The lower part of the Guandao 3 section is correlated with the Lower Guandao section using the distinctive thick reddish-colored beds and the conodont biostratigraphy of the 171–207 m interval (Sun et al., 2015), and using volcanic ash beds and facies patterns in its upper part. GR and filtered 17-m cycles (Gauss filter, passband of 0.06 ± 0.03 cycles/m) have 3 tuning options to eccentricity as discussed in Section 3.3. **Upper Chaohu**: Features of the Lower Guandao and Guandao 3 sections that may have correlative features to the **Chaohu** section (Fig. 3) are the conodont datums and reddish beds in the lower part, and magnetostratigraphy plus general GR signal and lithology patterns in the middle and upper parts (details in Appendix Section A.4.2). (For interpretation of the references to color in this figure legend, the reader is referred to the web version of this article.)

lation rate for the lowermost Anisian strata in which the 20-m cycles from 240 to 281 m are 405-kyr cycles. In this option, the sudden change in accumulation rate corresponds to the major shift in depositional setting across the Olenekian/Anisian boundary (OAB) at Guandao from thick-bedded carbonate interbedded with breccia beds to a thin-bedded carbonate (Fig. 6). Option #1 is allowed within the constraints from radio-isotopic dates within and above this interval and implies a 0.45-myr duration for the reversed-polarity zone across the OAB (Fig. 8). That 0.45-myr duration is 0.2-myr longer than its proposed cycle-scaled 0.25-myr duration in the Germanic Basin (Szurlies, 2007), but perhaps there may be missing cycles at a possible unconformity below the Stammem Beds of Solling Formation (Bachmann and Kozur, 2004).

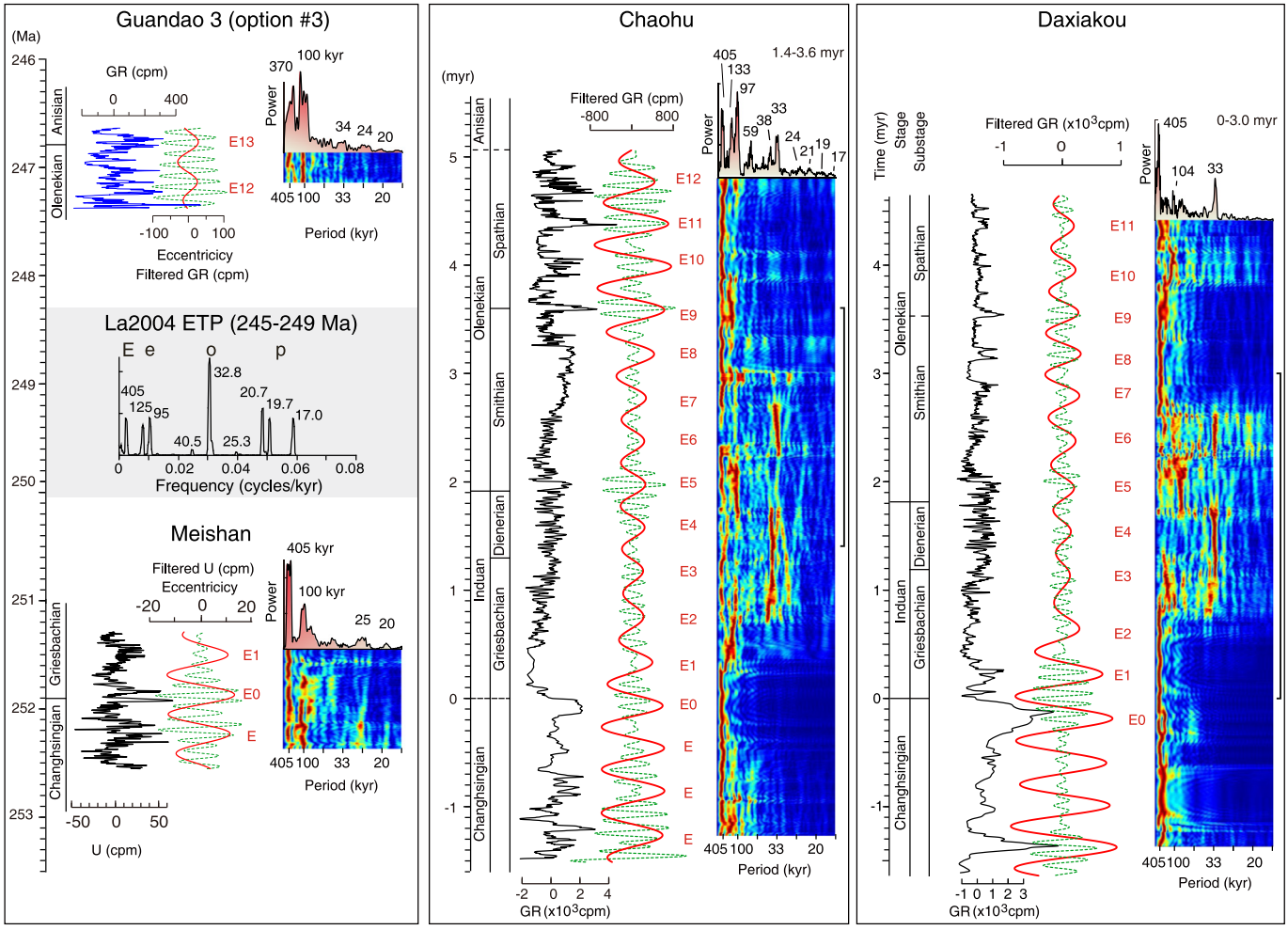

Fig. 7. Cyclostratigraphy of the Meishan, Chaohu, Daxiakou and Guandao sections of South China after tuning to the time domain. **Meishan**: the 100-kyr-tuned U series after subtracting a 66% weighted average with filtered 405-kyr (red, E) and 100-kyr (dashed green) cycles (Gauss filter, bandpass: 0.0025 ± 0.0001 and 0.01 ± 0.003 cycles/kyr, respectively). 2π MTM evolutive FFT using a 500-kyr sliding window and power spectrum are also shown. **Chaohu**: the 405-kyr-tuned GR series after subtracting 15% weighted average with filtered 405-kyr (red-colored "E" set) and 100-kyr (dashed green) cycles (Gauss filter, bandpass: 0.00248 ±0.0005 and 0.0100 ± 0.0025 cycles/kyr, respectively) with its evolutive FFT spectrum using a 500-kyr sliding window showing 2π MTM spectrum of Dienerian–Smithian (1.4–3.6 myr) after less a 35% weighted average. **Daxiakou**: the 405-kyr-tuned GR series after subtracting 25% weighted average with filtered 405-kyr (red, E) and 100-kyr (dashed green) cycles (Gauss filter, bandpass are as used at Chaohu) with evolutive FFT spectrum using a 500-kyr sliding window. 2π MTM spectrum of Griesbachian–Smithian (0–3 myr) is shown at the top after less a 25% weighted average. **Guandao**: the 405-kyr-tuned GR series after subtracting a 66% weighted average with filtered 405-kyr and 100-kyr cycles (the same procedure as applied at Meishan). 2π MTM evolutive FFT using a 500-kyr sliding window and power spectrum are also shown. **La2004 ETP**: Predicted eccentricity–obliquity-precession standardized time series of the La2004 ETP model (Laskar et al., 2004) from 245 to 249 Ma. (For interpretation of the references to color in this figure legend, the reader is referred to the web version of this article.)

Option #2 assumes a more steady accumulation rate, therefore postulates that there are seven 405-kyr cycles of fairly stable 17-m wavelength (Fig. 6). This Guandao Option #2 corresponds to the excluded Chaohu Option #2, but is still allowed within the constraints of the radio-isotopic dates (Lehrmann et al., 2006, 2015). However, Option #2 would imply a 0.9-myr duration for the reversed polarity zone across the OAB at Guandao, which is difficult to reconcile with its relatively narrow width or cycle-scaled duration in other global regions (e.g., Hounslow and Muttoni, 2010; Szurlies, 2007).

Option #3 assigns the 60-m peak as a single 405-kyr cycle, thereby implying a duration of ~250 kyr for the reversed-polarity zone across the OAB (Fig. 8 to match its cycle-scaled ~250-kyr duration in the Germanic Basin, Szurlies, 2007). However, this Option #3 (Fig. 6) is more difficult to reconcile with the span between radio-isotopic dates in this section (Lehrmann et al., 2006, 2015).

3.4. Floating astronomical time scale for Lower Triassic of South China

The 405-kyr eccentricity cycle has remained relatively stable over at least the past 250 myr due to great mass of Jupiter (Laskar et al., 2004), therefore is widely used as "405-kyr metronome" in the Cenozoic and Mesozoic (e.g., Hinnov and Hilgen, 2012). We also construct a floating ATS (Fig. 7) based on tuning to the filtered 405-kyr cycles with additional enhancement using the 100-kyr eccentricity cycles. The power spectrum of the 405-kyr-tuned GR series of the Chaohu section in the 1.4 to 3.6 myr interval (relative to "0" myr at the PTB) displays additional cycles with significant power at 133-kyr, 97-kyr, 59-kyr, 38-kyr, 33-kyr, 24-kyr, 21-kyr, 19-kyr and 17-kyr frequencies, which match the predicted Early Triassic astronomical terms (Fig. 7) (Laskar et al., 2004).

4. Discussion

4.1. Eccentricity–precession alternating with obliquity forcing during the Early Triassic

The evolutive spectra of the Chaohu and Daxiakou sections have comparable patterns. Eccentricity-precession signals dominate in the lower through middle Griesbachian, in the upper Smithian and in the middle through upper Spathian. In contrast, there are

two distinct chronostratigraphic intervals dominated by obliquity at both sections – the upper Griesbachian through Dienerian and the lower Spathian (Figs. 5 and 7). The interpretation that these even-spaced ~0.8-m bundles of carbonate-claystone are obliquity cycles is also supported by strong signals in the obliquity band in evolutive spectra in Figs. 5 and 7. Eccentricity-modulation of precession forcing are typically characterized by complex couplets and bundles (e.g. Fig. 3C), whereas obliquity forcing usually produces simple and fairly regular oscillations. The prominence of obliquity cycles during intervals during the Early Triassic has been reported from facies containing abundant oolites and thin parasequences in the Dawen and Dajiang sections from the Great Bank of Guizhou in the Nanpanjiang Basin near the Guandao section; and these may indicate equatorial atmospheric circulation (Yang and Lehrmann, 2003) or high-latitude influences on this low-latitude marine setting (e.g., Li et al., 2015, and in prep.).

4.2. Cycle-calibrated magnetostratigraphy and correlation to Germanic Basin

When combined with cyclostratigraphy, the magnetostratigraphic patterns provide a reliable timescale for intercontinental correlation. The continental deposits of the Lower Triassic of the Germanic Basin have distinctive facies oscillations interpreted as variable seasonal monsoon rainfall and runoff that was modulated by the 100-kyr eccentricity cycles (e.g., Bachmann and Kozur, 2004), therefore the duration of each of those polarity zone has been estimated by assigning these 100-kyr cycles to the oscillations in facies and to variances in GR (Szurlies, 2004, 2007). A similar synthesis of cycle-scaled polarity zones for the Germanic Basin compiled by Menning and Käding (2014) had suggested two very slightly different options, but we utilize the option that corresponds to the majority of the compilation by Szurlies (2004, 2007). This Germanic Basin magnetic-polarity pattern with its partial calibration of its brackish-water conchostracan zones to marine sections (e.g., Kozur and Weems, 2011) has been correlated to the main features of the magnetostratigraphies from other ammonite- and conodont-zoned outcrops in both Boreal and Tethyan realms (e.g., review by Hounslow and Muttoni, 2010).

The cycle-tuned durations of the main magnetostratigraphy zones from the Induan and the Spathian of Meishan and Chaohu are consistent with this astronomical-tuned Early Triassic magnetic polarity pattern derived from the terrestrial facies of the Germanic Basin. The base of the Triassic throughout the world occurs in the lowermost portion of a relatively long-duration normal-polarity magnetic zone (Hounslow and Muttoni, 2010). At Meishan, the Triassic part of this normal-polarity zone is 0.5 myr in duration according to cycle stratigraphy (Fig. 8), which is identical to both the ca. 0.5-myr duration derived from high-precision dating at this Meishan section (Burgess et al., 2014) and the cycle-tuned duration in the magnetostratigraphy of the Germanic Basin.

The middle-upper Induan of Chaohu is dominated by reversed polarity with a normal-polarity band in the upper Griesbachian. Our cycle-derived durations of 0.47 myr for Chaohu polarity zone Ch1r and 1.02 myr for Ch2n–Ch2r (corresponding to zones WP2–WP4 of Sun et al., 2009) are fit to the cycle-tuned durations for polarity zones of CG4r (0.45 myr) and CG5 (0.95 myr) of the Germanic Basin (Fig. 8).

The Smithian–Spathian boundary interval at Chaohu is dominated by normal-polarity zone MJ1n, which is similar to its signature in the Germanic Basin and composite marine magnetostratigraphy scales. Zone MJ4r of the uppermost Spathian corresponds to the reversed-polarity zone that includes the OAB in these scales (CG10r and LT9r in Fig. 8). The cycle-tuned durations of the pairs of polarity chrons through the Spathian at Chaohu and in the Germanic Basin are identical (Fig. 8). Indeed, within each of the main Spathian magnetic polarity zones, every one of the interpreted 100-kyr cycles in the Germanic Basin has a corresponding peak in relative clay enrichment in the Chaohu GR record (detailed in Section C.4 and Fig. C.5 of the Supplemental Information). These correlations indicate that the changing intensity of the monsoon rainfall/runoff in the interior basins of Pangea occurs in-step with changes in fluxes of clay onto the margins of the South China Plate. Therefore, this cycle-tuned magnetic polarity timescale can be used for precise projection of marine-based substages and biostratigraphic zones onto continental and high-latitude sedimentary deposits that have magnetostratigraphy.

4.3. Durations and ages of the Early Triassic substages and events

Tuning of these GR and U series to eccentricity cycles provides a floating ATS for the substages, main conodont zones, and magnetic polarity zones of the entire Early Triassic Epoch. Combining the uncertainties in placement of substage definitions with respect to variation of accumulation that is inherent within the 405-kyr cycle implies an uncertainty of about one 100-kyr (ca. ±0.1 myr) for most of these events within each section. The resulting floating ATS has durations of 1.4 ± 0.1 myr, 0.6 ± 0.1 myr, 1.7 ± 0.1 myr and 1.4 ± 0.1 myr for the Griesbachian, Dienerian, Smithian and Spathian substages, respectively, as defined in the main Chaohu and Guandao reference sections. The total duration of the Early Triassic Epoch is 5.1 ± 0.1 myr.

For calibration to numerical time, we anchored the PTB at Meishan to the 251.902 ± 0.024 Ma age of the PTB as interpolated by high-precision radio-isotope dating at its Meishan GSSP (Burgess et al., 2014). Cycle-tuned ages of ash beds in the Griesbachian at Meishan fit those radio-isotope dates (Fig. 2B). This anchored ATS projects ages of 250.5 ± 0.1 Ma, 249.9 ± 0.1 Ma, 248.2 ± 0.1 Ma and 246.8 ± 0.1 Ma for the base Dienerian, base Smithian, base Spathian and base Anisian, respectively (Fig. 9).

4.3.1. Cycle-tuned duration of the end-Permian mass extinction (EPME) interval

The pattern and timing of the EPME are hotly debated topics. Shen et al. (2011) proposed that marine biodiversity suffered a sharp one-step extinction over a very narrow interval at Meishan from the top of Bed 24e through Bed 28. In comparison, other examinations of the ecological changes and biodiversity across the PTB suggest a two-step extinction pattern, in which the first step at the top of Bed 24e was marked by the extinction of 57% of the species, then a stable situation that was truncated when 71% of the surviving species underwent extinction at the top of Bed 28 (Song et al., 2013b). Regardless whether it was a one- or two-phase extinction, all research agrees that EPME interval at Meishan from the onset of the carbon isotope negative excursion at the top of Bed 24e through Bed 28 represents a critical major turnover of Earth life. Constraints from radio-isotopic dating at Meishan indicate that the EPME spanned an interval of only 60 ± 48 kyr (Burgess et al., 2014).

Cyclostratigraphy estimates for the span of this major EPME turnover at the Shangsi section in Sichuan, which used a different definition of the extinction interval, range from 700 kyr (Huang et al., 2011) to 380 kyr. At the Meishan GSSP, an interpretation and 405-kyr-cycle tuning of the oscillations in magnetic susceptibility seemed to imply a duration of ~80 kyr for the EPME interval (Beds 25–28) (Wu et al., 2013). Our application of 100-kyr tuning to Meishan indicates that the EPME spans less than 40% of a 100-kyr cycle, therefore <40 kyr (Fig. 2). The sharp 5‰ negative excursion in $\delta^{13}C$ isotopes starts abruptly within Bed 24e and ends in Bed 25, a span of only 5 cm, is less than 6% of a 100-kyr cycle or <6 kyr, which is consistent with a cycle-tuned <30-kyr duration in the Carnic Alps of Austria (Rampino et al., 2000) and

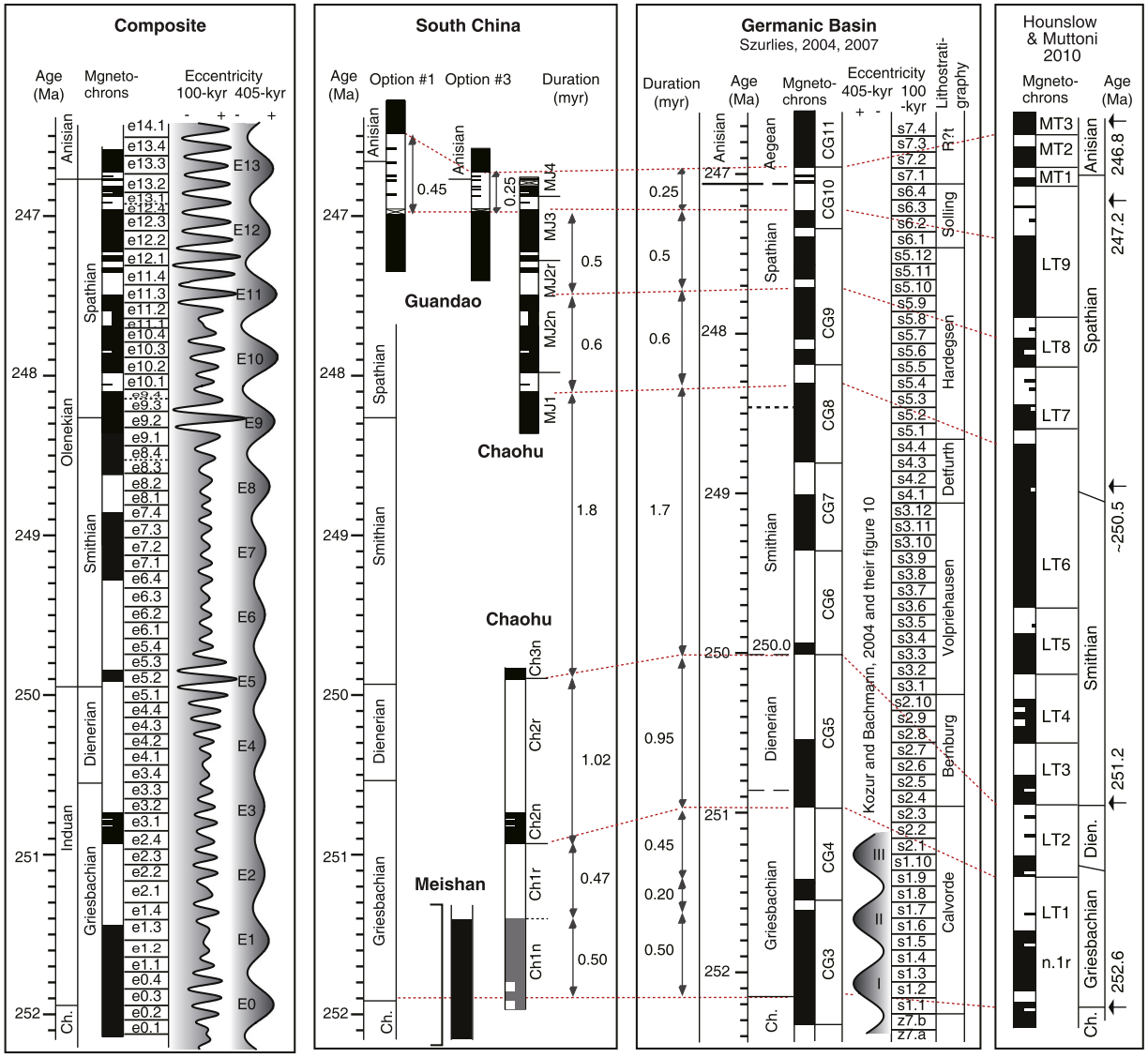

Fig. 8. Cycle-tuned magnetic polarity reference scales for the Early Triassic. Left-most column is our composite cycle-tuned polarity pattern derived from the Griesbachian–Dienerian and Spathian of South China and from the Smithian of Germanic Basin. The South China column has cycle-tuned magnetostratigraphies from the Meishan section (Li and Wang, 1989), the lower Chaohu section (Sun et al., 2009 as reinterpreted in Appendix Section C and Appendix Fig. C.4), and from the upper Smithian through Spathian of Chaohu (this study). Two options are shown for the cycle-scaled magnetostratigraphy across the Olenekian/Anisian boundary at Guandao (Lehrmann et al., 2006) as discussed in Section 3.3. The main South China zones are correlated to the 100-kyr cycle-tuned polarity pattern from the Germanic Basin (Bachmann and Kozur, 2004; Szurlies, 2004, 2007; as reviewed by Ogg, 2012) and to the "relative-thickness-scaled" magnetostratigraphy synthesis of Hounslow and Muttoni (2010). Details of these correlations are discussed in Section 4.2 and an enlargement of the Spathian correlations is in Appendix Section C.5. The age model for the Germanic Basin reference scale had been anchored to a base-Triassic date of 252.17 Ma (Shen et al., 2011), which was re-dated as 251.9 Ma (Burgess et al., 2014) as shown in the South China and the Composite scales. Selected radiometric dates used by Hounslow and Muttoni (2010) on their scale were from Mundil et al. (2004), Galfetti et al. (2007), Ovtcharova et al. (2006) and Lehrmann et al. (2006), which were published before the revised EARTHTIME tracer solutions (Burgess et al., 2014).

within the constraints from radio-isotope dating of $<20 \pm 10$ kyr (Shen et al., 2011) or 2.1–18.8 kyr (Burgess et al., 2014). These results confirm the short-lived nature of the EPME. Considering that estimates from the highly condensed Meishan section are probably distorted by non-linear recording by these sediments of the ecological and climatic responses, we predict that, when further higher-resolution studies are achieved in more expanded sections, the EPME and this negative excursion in $\delta^{13}C$ isotopes were even sharper catastrophic events.

4.3.2. *Griesbachian duration and implication for relative sediment accumulation rates across the Permian–Triassic boundary*

The duration of the Griesbachian Substage can be estimated by combining cyclostratigraphies of Meishan and Chaohu. Unfortunately, recognition of cycle "E0" (the first 405-kyr eccentricity cycle of the Triassic) and its constituent 100-kyr "e" cycles at both Chaohu and Daxiakou is distorted through both a condensation in the basal Griesbachian and a downward shift in the apparent peak of 405-kyr Cycle "E0" due to a sharp drop from elevated GR values in the Permian black shale to low-GR values in carbonate-rich basal Triassic (Fig. 5). The magnetostratigraphy of the Chaohu succession also indicates that the majority of the normal-polarity zone of the lower Griesbachian is highly condensed (Hounslow and Muttoni, 2010; Sun et al., 2009). In comparison, Meishan does not have this uppermost Permian black shale, therefore the Cycle "E0" recorded in GR and U is well-recognized and an allows placement of the base of the Griesbachian (PTB) at just 40 kyr (40% of a 100-kyr cycle) before the peak of "E0" (Fig. 2). In the Germanic Basin, the estimated PTB is also slightly less than 100 kyr earlier than the peak of the first 405-kyr cycle (I) of the Triassic (Fig. 8).

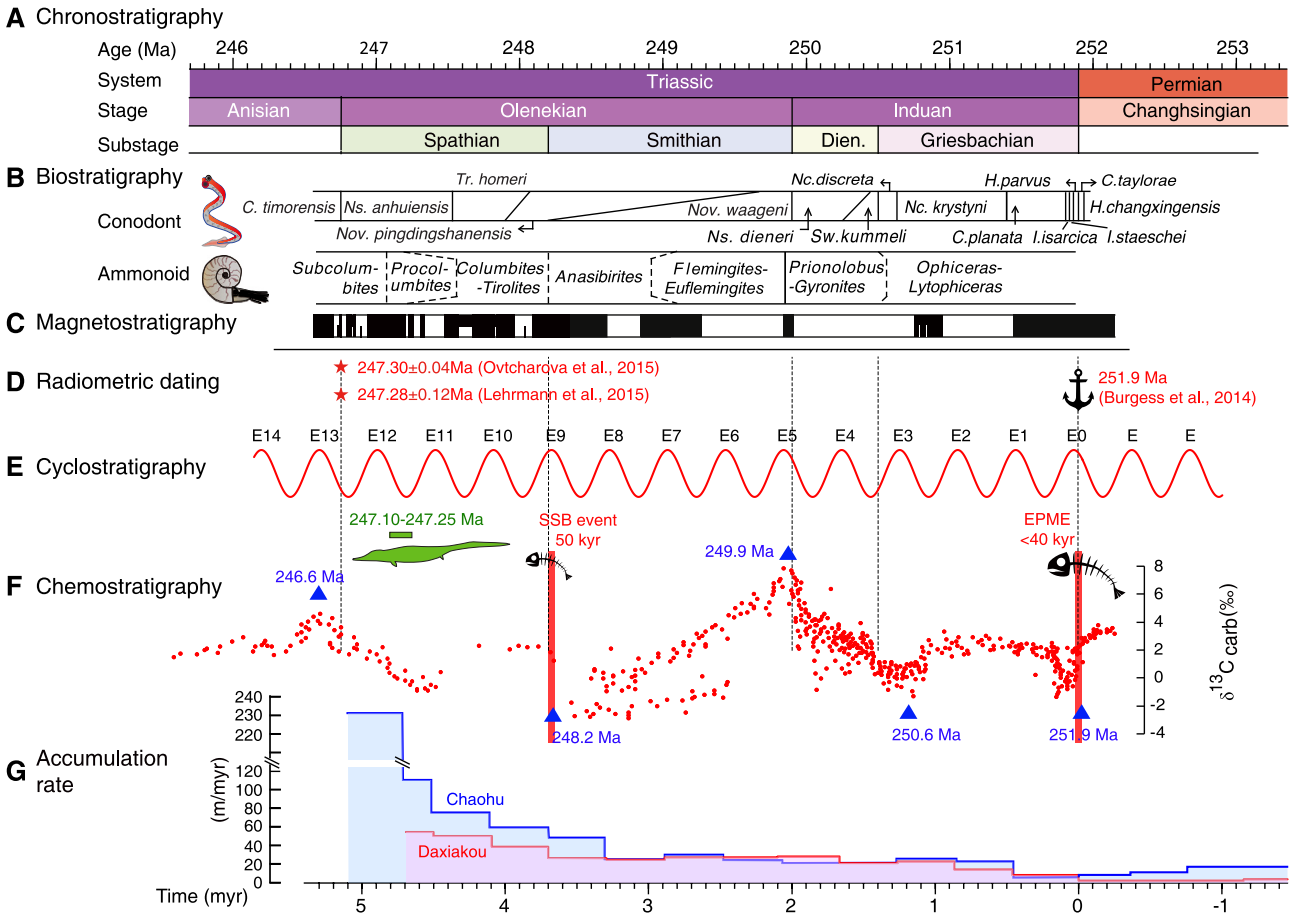

Fig. 9. Summary of Early Triassic timescale of South China. **A**. Chronostratigraphy and **B**. biostratigraphy are based on Figs. 2, 5 and 6 and detailed in Appendix Fig. B.1. **C**. Magnetostratigraphy is from Fig. 8. **D**. Radiometric dates are from Burgess et al. (2014), Lehrmann et al. (2015) and Ovtcharova et al. (2015). **E**. 405-kyr cycles is based on Figs. 7 and 8. **F**. $\delta^{13}C$ data are from Great Bank of Guizhou, South China (Payne et al., 2004) shown with excursions with age. The end-Permian extinction and the Smithian–Spathian boundary (SSB) event are marked by a fish skeleton. Reptile beds at Chaohu (Motani et al., 2015) are indicated by the green silhouette and age-span bar. **G**. Accumulation rates (405-kyr averages) of the Chaohu and Daxiakou sections increased gradually in the Griesbachian through Smithian, then surged in the Spathian from an increased influx of carbonate. (For interpretation of the references to color in this figure legend, the reader is referred to the web version of this article.)

The lower Griesbachian *Hindeodus parvus*, *Isarcicella staeschei*, *I. isarcica* and *C. planata* zones within this normal-polarity zone at Meishan are interpreted to span 500 kyr (Fig. 8). A ~500 kyr span for these four conodont zones is also implied by the radio-isotopic dating of these cycles at Meishan (Burgess et al., 2014) (Fig. 2). The cycle-tuned duration of the basal-Triassic normal-polarity zone at Meishan is also identical with the cycle-tuned magnetostratigraphy of the Germanic basin (Kozur and Weems, 2011).

The upper Griesbachian has a complete and undistorted record at both Chaohu and Daxiakou. The base of the Dienerian is ~150 kyr after the peak of Cycle "E3" implying a 1.4-myr duration for the Griesbachian Substage (Fig. 7). The *Neoclarkina krystyni* and *Neoclarkina discreta* conodont zones span ca. 770 kyr and 130 kyr, respectively, based on our ATS (Appendix Section B.2 for details).

Some studies have suggested that there had been surges in terrestrial weathering and in sediment and nutrient fluxes into the marine environments at the EPME, and this played a role in the delayed recovery. These calculations depended on the relative durations of the Changhsingian and Griesbachian substages (C:G duration ratio). For example, using a C:G duration ratio of 3.4:0.7 myr would imply a global 7× average increase in influx of terrigenous sediment during the Griesbachian relative to the Changhsingian based on sediment thicknesses in 16 marine sections in Neotethys, Paleotethys and Panthalassa oceans (Algeo and Twitchett, 2010). However, if the C:G duration ratio is 1.9:1.4 myr based on cyclostratigraphy interpretations (Szurlies, 2007; Wu et al., 2013), then the increase in average terrigenous influx would be reduced to a factor of 2×, which is still important but not as dramatic. Moreover, the accumulation rates estimated from the high-resolution ATS suggest a gradual, rather than abrupt, change during and after the EPME at Meishan, Chaohu and Daxiakou (Fig. 9).

4.3.3. Dienerian

The Dienerian Substage spans a 0.6 myr at both the Chaohu and Daxiakou sections based on the defining conodont zones (Zhao et al., 2013, 2007). The Dienerian and the Induan ended 50 kyr before the peak of Cycle "E5" at the Olenekian GSSP candidate section of Chaohu. However, the first occurrence (FO) of the marker conodont *Nov. waageni* is ~50 kyr earlier at Daxiakou than at Chaohu. Therefore, a 2.0 ± 0.1 myr total duration for the Induan Stage is indicated.

Our ATS-derived Induan duration is significantly longer than ~1.1-myr Induan duration estimated from magnetic susceptibility logs in those same Chaohu and Daxiakou sections by Guo et al. (2008) and Wu et al. (2012). Their interpretation was influenced by an assumption that in these low-latitude sections the dominant ~0.8-m-scale couplets should be precession cycles. In contrast, our use of GR logging enabled recognition of the broader 10-m long-eccentricity cycles which also implied that the even-spaced ~0.8-m cycles represented obliquity cycles (Section 4.1). Furthermore, the cycle-scaled magnetostratigraphy from the Diene-

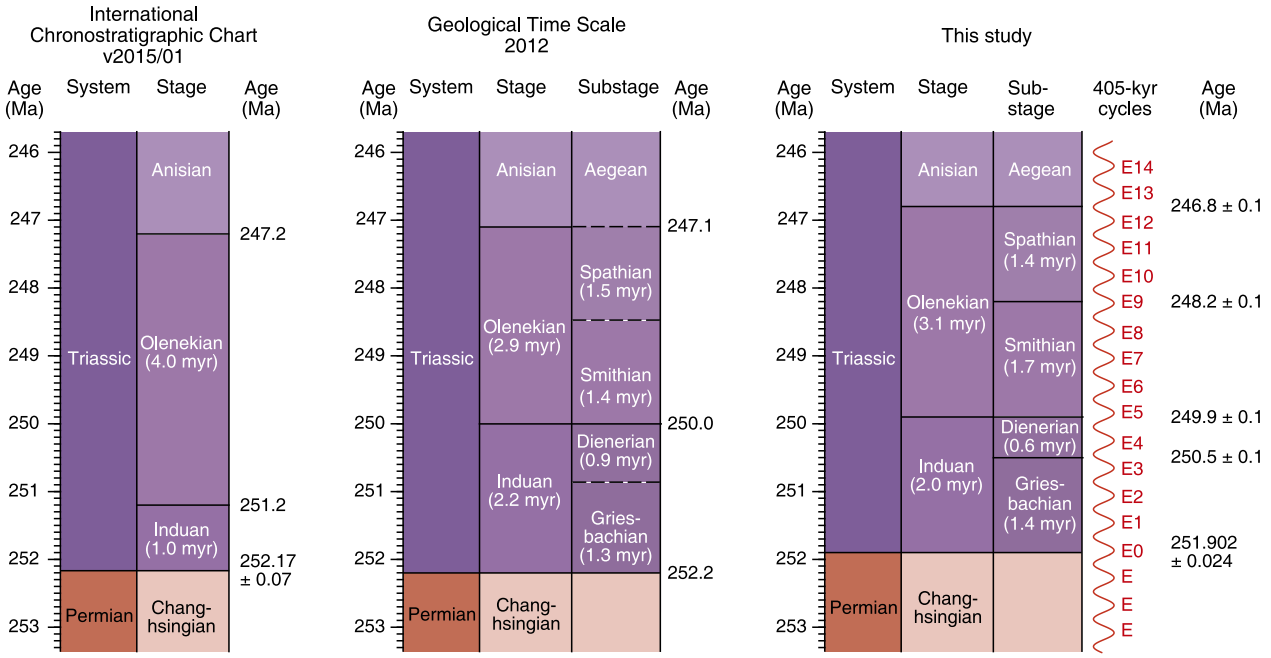

Fig. 10. Comparisons of the Early Triassic age models of the International Chronostratigraphic Chart v2015/01 (http://www.stratigraphy.org), of the Geologic Time Scale 2012 (Ogg, 2012) and of this study.

rian of Chaohu matches the cycle-scaled polarity pattern from the Germanic Basin (Fig. 8).

4.3.4. Smithian and the Smithian–Spathian boundary (SSB) event

The SSB event represents one of the most severe bio-crises after the EPME. Marine and terrestrial life experienced a major turnover coincident with a strong perturbation in the carbon cycle (Payne et al., 2004; Tong et al., 2007), an widespread oceanic euxinia (Grasby et al., 2013) and a late Smithian thermal maximum (Sun et al., 2012). At Chaohu, a shift in $\delta^{13}C$ from $-2‰$ to $4‰$ is the key indicator of the SSB event near the FAD of the conodont *Nov. pingdingshanensis* (Appendix Fig. A.4) (Tong et al., 2007). This level at Chaohu is just after the peak of Cycle "E9", therefore the Smithian Substage spans 1.7 ± 0.1 myr (Fig. 9). The Smithian duration was also estimated as ~1.6 myr in the Germanic Basin (Szurlies, 2007), but both of the stage limits in those terrestrial deposits are offset older by 3 to 4 short-eccentricity cycles from the conodont-based ones used in our study. The SSB event occurred 3.7 myr after the EPME, and the duration of the $\delta^{13}C$ shift is ~50 kyr.

4.3.5. Spathian and age of marine reptiles at Chaohu

Due to the lack of conodonts and a potentially truncated magnetostratigraphy in the uppermost Spathian to assign the Olenekian/Anisian boundary (OAB) at Chaohu, the duration for the Spathian Substage is from correlation of the upper Spathian section of Chaohu to the OAB interval at Guandao using reddish beds, lithological patterns, GR and magnetostratigraphy (Fig. 6). The base of the Anisian at Guandao at the appearance of conodont *Chiosella timorensis*, the proposed conodont marker for the Early–Middle Triassic boundary, is positioned ~150-kyr before the peak of Cycle "E13". Therefore, the Spathian spans 1.4 ± 0.1 myr. Szurlies (2007) had estimated a Spathian duration of 1.9 myr, but he estimated that the Smithian–Spathian boundary was at a lower level in those non-marine deposits, and correlating his cycle-tuned magnetostratigraphy of the Germanic Basin to Smithian–Spathian ammonoid-zoned sections of the Arctic regions indicates a ca. 1.5-myr duration (Ogg, 2012).

The Chaohu section yields nearly 100 skeletons of four genera of large marine reptiles that are considered to mark the significant recovery of ecosystem after the EPME (Ji et al., 2015; Motani et al., 2015). These reptile beds occur within the middle Spathian *Procolumbites* ammonoid Zone (Ji et al., 2015; Motani et al., 2015). Our ATS constrains the age of these Chaohu reptile beds to be ca. 4.7 myr after the EPME, or between 247.10 and 247.25 Ma (green bar in Fig. 9).

4.3.6. Duration of Early Triassic Epoch and projected age for the base of the Anisian Stage

The duration of the Early Triassic Epoch in both the South China and the Germanic Basin cycle-tuned scales is 5.1 ± 0.1 myr. The South China sections indicate durations of 2.0 ± 0.1 myr and 3.1 ± 0.1 myr for the Induan and Olenekian stages. These spans are remarkably similar to the 2.2-myr and 2.9-myr durations from the correlation of the cycle-tuned magnetostratigraphy of the Germanic Basin (Szurlies, 2004, 2007) to ammonite- and conodont-dated sections (Hounslow and Muttoni, 2010) as used in GTS2012 (Ogg, 2012). In contrast, the International Chronostratigraphic Chart of 2015 (ICS2015) displays 1.0- and 4.0-myr durations for the Induan and Olenekian stages (Fig. 10). This ICS2015 chart did not document how these estimates were derived, but perhaps the compact span for the Induan Stage resulted from comparing a base-Triassic dating of ca. 252.2 Ma (Shen et al., 2011) to an earlier dating of 251.2 ± 0.1 Ma for a lower Smithian ash bed (Galfetti et al., 2007) that had used different standards that are difficult to reconcile with the revised EARTHTIME protocols and tracer (Burgess et al., 2014).

Guandao has several ash beds near the OAB that have been dated using single zircons. Using mean dates derived from a subset of U–Pb dates from those zircons yields a linear-interpolated estimate of 247.28 ± 0.12 Ma for the FAD of conodont *Ch. timorensis* (Lehrmann et al., 2015). Another study with high-resolution dating of the OAB from the conodont-rich Monggan section of Guangxi highlighted the uncertainty of radiometric dating due to post-crystallization lead loss and unknown crystallization history of individual zircons, coupled with subjective interpretations of which zircons to include in the subset used for the statistical date

(Ovtcharova et al., 2015). Interpolation of dated ash-layers bracketing the OAB at Monggan/Wantou projects the FAD of *Chiosella timorensis* as 247.31 ± 0.06 Ma (Ovtcharova et al., 2015). In comparison, our cycle-tuned age for the FAD of *Chiosella timorensis* based on anchoring to the base-Triassic dating is 246.8 ± 0.1 Ma.

Why is the cycle-tuned duration of 5.1-myr for the Early Triassic nearly 0.4 myr longer than the 4.6-myr difference of two U–Pb ages for its base at the PTB of 251.9 Ma (Burgess et al., 2014) and its top at the base of the Anisian Stage of 247.3 Ma (Lehrmann et al., 2015; Ovtcharova et al., 2015)? This identical problem arises for the 5.1-myr span for the Germanic Basin cyclostratigraphy based on recognition of 100-kyr cycles across the basin (Szurlies, 2007). Some possibilities are (1) the subjective methods of selecting which zircon dates are incorporated into the published best-estimate "mean" dates, which often only incorporates less than 30% of the dated zircons, needs to be re-examined, as is discussed with some excellent out-of-sequence examples by Ovtcharova et al. (2015); (2) the base-Anisian date may be too old because of pre-eruption zircons in the base-Anisian ages, or the PTB date from Meishan may be too young due to lead-loss (these potential artifacts for some interpreted dates from the Monggan/Wantou section are also examined in Ovtcharova et al., 2015); (3) one of the fourteen compiled 405-kyr long-eccentricity cycles in the Early Triassic (E0–E13) may be incorrect interpretation of a cycle that is actually a 100-kyr short-eccentricity cycle; although this would require a simultaneous accidental interpreting of "too many" cycles in the independent Germanic Basin succession; and/or (4) both the radioisotopic and the cyclostratigraphic methods in all studies have larger uncertainties than is usually assumed by those workers (see Ovtcharova et al., 2015, and the introductory discussion of our paper). To resolve this question will require both additional standardized radio-isotopic dating of the boundaries of the Early Triassic stages in sections outside of South China, and verification of the cycle scalings of the Early Triassic magnetic polarity zones and substages in regions other than in Germany and China.

5. Conclusions

A high-resolution astronomical time scale for the end-Permian mass extinction and the Early Triassic Epoch that is constrained by radioisotopic dating, conodont datums, magnetic polarity zones and chemostratigraphy, has been established from the consistent cyclostratigraphy recorded in four reference marine sections of South China. Five main conclusions are as follows:

1. High-resolution astronomical time scale of the Early Triassic indicates durations of 1.4 ± 0.1, 0.6 ± 0.1, 1.7 ± 0.1 and 1.4 ± 0.1 myr for the Griesbachian, Dienerian, Smithian and Spathian substages, respectively, with a uncertainties of less than one-half of a 405-kyr eccentricity cycle in the main Chaohu and Guandao reference sections. The Early Triassic Epoch spans 5.1 ± 0.1 myr. When anchored to the interpolated 251.902 ± 0.024 Ma date for the base of the Triassic (Burgess et al., 2014), the ages of the base-Dienerian, base-Smithian, base-Spathian and base-Anisian are 250.5 ± 0.1, 249.9 ± 0.1, 248.2 ± 0.1 and 246.8 ± 0.1 Ma, respectively (Fig. 10).
2. Constrained by high-resolution radio-isotopic dates near the PTB at the Meishan GSSP section, the oscillations in the GR and U series were interpreted as 100-kyr short-eccentricity cycles. These imply that the end-Permian mass extinction interval from the top of Bed 24e to Bed 28 at Meishan lasted less than 40 kyr. The abrupt 5‰ negative $\delta^{13}C$ excursion that starts within Bed 24e and ends in Bed 25 spans less than 6 kyr.
3. There are no significant enhanced accumulation rates of sediments following the end-Permian extinction and environmental disruption at these cycle-tuned South China sections. The postulated surge of terrigenous sediment fluxes occurring worldwide during the early Griesbachian as a result of increased weathering from elevated temperatures is not observed in this region; and this revised Early Triassic time scale would also significantly reduce the calculated fluxes in other regions.
4. The Smithian–Spathian Boundary (SSB) event occurred 3.7 myr after the EPME. The duration of the $\delta^{13}C$ shift across the SSB is 50 kyr.
5. The cycle-tuned magnetostratigraphy from terrestrial deposits in the Germanic basin (Szurlies, 2004, 2007) is consistent with the majority of the durations of major polarity zones recorded in these marine sections of South China. The changing intensity of the rainfall of these mega-monsoons in the interior basins of Pangea occurs in-step with changes in fluxes of clay onto the margins of the Yangtze Platform of South China. This verification implies that the main polarity zones of this cycle-tuned magnetostratigraphy can be used for projecting precise marine-based substages and biostratigraphic zones and high-precision durations onto continental and high-latitude sedimentary deposits.

Acknowledgements

Haishui Jiang, Shizhen Jia, Na Gao, Xiaoqing Liu, Baiyu Qu, Weizhe Chen, Wei Tian, Xiaokun Huang and Yonglin Chen of China University of Geosciences (Wuhan) are gratefully acknowledged for field assistance. We thank reviewers Gerhard Bachmann, Wan Yang and one anonymous reviewer for their specific comments, excellent questions and instructive suggestions. This study was supported by the National Natural Science Foundation of China (No. 41322013 and 41272023), the Program of Introducing Talents of Discipline to Universities (No. B14031), the Program for New Century Excellent Talents in University (NCET-11-0723), the Chinese 973 Program (2012CB822003) and, for J.O., by a visiting professorship at the State Key Laboratory of Geobiology and Environmental Geology funded by the Overseas Distinguished Teacher Program of the Ministry of Education (MS2013ZGDZ[WH]028). M. Li acknowledges the China Scholarship Council for Ph.D. work at Johns Hopkins University, USA and the Geologic TimeScale Foundation for work at Purdue University, USA. Magnetostratigraphy analyses were undertaken at (1) the Black Mountain paleomagnetism laboratory (Australian National University) in Canberra under the guidance of David Heslop and Xiang Zhao, for which Y.Z.'s stay was funded by the Geologic TimeScale Foundation (USA), (2) Laboratory for Paleomagnetism and Environmental Magnetism, China University of Geosciences (Beijing) under the direction of Shihong Zhang, and (3) Institute of Geomechanics, Chinese Academy of Geological Sciences in Beijing under the supervision of Zhiming Sun.

Appendix A. Supplementary material

Supplementary material related to this article can be found online at http://dx.doi.org/10.1016/j.epsl.2016.02.017. These data include the Google map of the most important areas described in this article.

References

Algeo, T.J., Twitchett, R.J., 2010. Anomalous Early Triassic sediment fluxes due to elevated weathering rates and their biological consequences. Geology 38, 1023–1026. http://dx.doi.org/10.1130/G31203.1.

Bachmann, G., Kozur, H., 2004. The Germanic Triassic: correlations with the international chronostratigraphic scale, numerical ages and Milankovitch cyclicity. Hallesches Jahrb. Geowiss. B 26, 17–62. http://public.bibliothek.uni-halle.de/index.php/hjg/article/download/1673/1772.

Bowring, S.A., Erwin, D.H., Jin, Y.G., Martin, M.W., Davidek, K., Wang, W., 1998. U/Pb zircon geochronology and tempo of the end-Permian mass extinction. Science 280, 1039–1045. http://dx.doi.org/10.1126/science.280.5366.1039.

Burgess, S.D., Bowring, S., Shen, S.-z., 2014. High-precision timeline for Earth's most severe extinction. Proc. Natl. Acad. Sci. USA 111, 3316–3321. http://dx.doi.org/10.1073/pnas.1317692111.

Chen, Z.-Q., Benton, M.J., 2012. The timing and pattern of biotic recovery following the end-Permian mass extinction. Nat. Geosci. 5, 375–383. http://dx.doi.org/10.1038/ngeo1475.

Cleveland, W.S., 1979. Robust locally weighted regression and smoothing scatterplots. J. Am. Stat. Assoc. 74, 829–836. http://dx.doi.org/10.1080/01621459.1979.10481038.

Feng, Z., Bao, Z., Li, S., 1997. Lithofacies Paleogeography of Middle and Lower Triassic of South China. Petroleum Industry Press, Beijing.

Galfetti, T., Bucher, H., Ovtcharova, M., Schaltegger, U., Brayard, A., Brühwiler, T., Goudemand, N., Weissert, H., Hochuli, P.A., Cordey, F., Guodun, K., 2007. Timing of the Early Triassic carbon cycle perturbations inferred from new U–Pb ages and ammonoid biochronozones. Earth Planet. Sci. Lett. 258, 593–604. http://dx.doi.org/10.1016/j.epsl.2007.04.023.

Goudemand, N., Orchard, M.J., Bucher, H., Jenks, J., 2012. The elusive origin of Chiosella timorensis (Conodont Triassic). Geobios 45, 199–207. http://dx.doi.org/10.1016/j.geobios.2011.06.001.

Grasby, S.E., Beauchamp, B., Embry, A., Sanei, H., 2013. Recurrent Early Triassic ocean anoxia. Geology 41, 175–178. http://dx.doi.org/10.1130/G33599.1.

Guo, G., Tong, J., Zhang, S., Zhang, J., Bai, L., 2008. Cyclostratigraphy of the Induan (Early Triassic) in West Pingdingshan Section, Chaohu, Anhui Province. Sci. China, Ser. D 51, 22–29. http://dx.doi.org/10.1007/s11430-007-0156-z.

Hays, J.D., Imbrie, J., Shackleton, N.J., 1976. Variations in the Earth's orbit: pacemaker of the Ice Ages. Science 194, 1121–1132. http://dx.doi.org/10.1126/science.194.4270.1121.

Hinnov, L.A., 2013. Cyclostratigraphy and its revolutionizing applications in the earth and planetary sciences. Geol. Soc. Am. Bull. 125, 1703–1734. http://dx.doi.org/10.1130/B30934.1.

Hinnov, L., Hilgen, F.J., 2012. Cyclostratigraphy and astrochronology. In: Gradstein, F., Ogg, J., Schmitz, M., Ogg, G. (Eds.), The Geologic Time Scale 2012. Elsevier, pp. 63–83.

Hounslow, M.W., Muttoni, G., 2010. The geomagnetic polarity timescale for the Triassic: linkage to stage boundary definitions. Geol. Soc. Spec. Publ. 334, 61–102. http://dx.doi.org/10.1144/SP334.4.

Huang, C., Tong, J., Hinnov, L., Chen, Z.Q., 2011. Did the great dying of life take 700 k.y.? Evidence from global astronomical correlation of the Permian–Triassic boundary interval. Geology 39, 779–782. http://dx.doi.org/10.1130/G32126.1.

Ji, C., Zhang, C., Jiang, D.-y., Bucher, H., Motani, R., Tintori, A., 2015. Ammonoid age control of the Early Triassic marine reptiles from Chaohu (South China). Palaeoworld 24, 277–282. http://dx.doi.org/10.1016/j.palwor.2014.11.009.

Kodama, K.P., Hinnov, L., 2014. Rock Magnetic Cyclostratigraphy. Wiley–Blackwell.

Kozur, H.W., Bachmann, G.H., 2008. Updated correlation of the Germanic Triassic with the Tethyan scale and assigned numeric ages. Ber. Geol. B–A 76, 53–58. http://www.landesmuseum.at/datenbanken/digilit/?serienr=20624.

Kozur, H.W., Weems, R.E., 2011. Detailed correlation and age of continental late Changhsingian and earliest Triassic beds: implications for the role of the Siberian Trap in the Permian–Triassic biotic crisis. Palaeogeogr. Palaeoclimatol. Palaeoecol. 308, 22–40. http://dx.doi.org/10.1016/j.palaeo.2011.02.020.

Laskar, J., Robutel, P., Joutel, F., Gastineau, M., Correia, A.C.M., Levrard, B., 2004. A long-term numerical solution for the insolation quantities of the Earth. Astron. Astrophys. 428, 261–285. http://dx.doi.org/10.1051/0004-6361:20041335.

Lehrmann, D.J., Ramezani, J., Bowring, S.A., Martin, M.W., Montgomery, P., Enos, P., Payne, J.L., Orchard, M.J., Hongmei, W., Jiayong, W., 2006. Timing of recovery from the end-Permian extinction: geochronologic and biostratigraphic constraints from south China. Geology 34, 1053–1056. http://dx.doi.org/10.1130/G22827A.1.

Lehrmann, D.J., Wei, J., Enos, P., 1998. Controls on facies architecture of a large Triassic carbonate platform: the Great Bank of Guizhou, Nanpanjiang Basin, South China. J. Sediment. Res. 68, 311–326. http://archives.datapages.com/data/sepm/journals/v66-67/data/068/068002/0311.HTM.

Lehrmann, D.J., Stepchinski, L., Altiner, D., Orchard, M.J., Montgomery, P., Enos, P., Ellwood, B.B., Bowring, S.A., Ramezani, J., Wang, H., Wei, J., Yu, M., Griffiths, J.D., Minzoni, M., Schaal, E.K., Li, X., Meyer, K.M., Payne, J.L., 2015. An integrated biostratigraphy (conodonts and foraminifers) and chronostratigraphy (paleomagnetic reversals, magnetic susceptibility, elemental chemistry, carbon isotopes and geochronology) for the Permian–Upper Triassic strata of Guandao section, Nanpanjiang Basin, south China. J. Asian Earth Sci. 108, 117–135. http://dx.doi.org/10.1016/j.jseaes.2015.04.030.

Li, H., Wang, J., 1989. Magnetostratigraphy of Permo–Triassic boundary section of Meishan of Changxing, Zhejiang. Sci. China 8, 652–658.

Li, M., Huang, C., Hinnov, L., 2015. Intermittent obliquity-forced climate during the Early Triassic. Abstr. Program – Geol. Soc. Am. 47, 697. http://dx.doi.org/10.13140/RG.2.1.2404.4887.

Mann, M.E., Lees, J.M., 1996. Robust estimation of background noise and signal detection in climatic time series. Clim. Change 33, 409–445. http://dx.doi.org/10.1007/BF00142586.

Menning, M., Käding, K.-C., 2014. Magnetostratigraphie, Zyklostratigraphie, geologische Zeitskala und Nomenklatur des Buntsandstein von Mitteleuropa. In: Lepper, J., Röhling, H.-G. (Eds.), Stratigraphie von Deutschland XI. Buntsandstein. Deutschen Gesellschaft für Geowissenschaften, pp. 165–212.

Motani, R., Jiang, D.-Y., Chen, G.-B., Tintori, A., Rieppel, O., Ji, C., Huang, J.-D., 2015. A basal ichthyosauriform with a short snout from the Lower Triassic of China. Nature 517, 485–488. http://dx.doi.org/10.1038/nature13866.

Mundil, R., Ludwig, K.R., Metcalfe, I., Renne, P.R., 2004. Age and timing of the Permian mass extinctions: U/Pb dating of closed-system zircons. Science 305, 1760–1763. http://dx.doi.org/10.1126/science.1101012.

Ogg, J.G., 2012. Triassic. In: Gradstein, F., Ogg, J., Schmitz, M., Ogg, G. (Eds.), The Geologic Time Scale 2012. Elsevier, pp. 681–730, Chapter 25.

Ovtcharova, M., Bucher, H., Schaltegger, U., Galfetti, T., Brayard, A., Guex, J., 2006. New Early to Middle Triassic U–Pb ages from South China: calibration with ammonoid biochronozones and implications for the timing of the Triassic biotic recovery. Earth Planet. Sci. Lett. 243, 463–475. http://dx.doi.org/10.1016/j.epsl.2006.01.042.

Ovtcharova, M., Goudemand, N., Hammer, Ø., Guodun, K., Cordey, F., Galfetti, T., Schaltegger, U., Bucher, H., 2015. Developing a strategy for accurate definition of a geological boundary through radio-isotopic and biochronological dating: the Early–Middle Triassic boundary (South China). Earth-Sci. Rev. 146, 65–76. http://dx.doi.org/10.1016/j.earscirev.2015.03.006.

Paillard, D., Labeyrie, L., Yiou, P., 1996. Macintosh program performs time-series analysis. Eos Trans. AGU 77, 379. http://dx.doi.org/10.1029/96EO00259.

Payne, J.L., Lehrmann, D.J., Wei, J., Orchard, M.J., Schrag, D.P., Knoll, A.H., 2004. Large perturbations of the carbon cycle during recovery from the end-Permian extinction. Science 305, 506–509. http://dx.doi.org/10.1126/science.1097023.

Rampino, M.R., Prokoph, A., Adler, A., 2000. Tempo of the end-Permian event: high-resolution cyclostratigraphy at the Permian–Triassic boundary. Geology 28, 643–646. http://dx.doi.org/10.1130/0091-7613(2000)28<643:TOTEEH>2.0.CO;2.

Ruffell, A., Worden, R., 2000. Palaeoclimate analysis using spectral gamma-ray data from the Aptian (Cretaceous) of southern England and southern France. Palaeogeogr. Palaeoclimatol. Palaeoecol. 155, 265–283. http://dx.doi.org/10.1016/S0031-0182(99)00119-4.

Schnyder, J., Ruffell, A., Deconinck, J.-F., Baudin, F., 2006. Conjunctive use of spectral gamma-ray logs and clay mineralogy in defining late Jurassic–early Cretaceous palaeoclimate change (Dorset, U.K.). Palaeogeogr. Palaeoclimatol. Palaeoecol. 229, 303–320. http://dx.doi.org/10.1016/j.palaeo.2005.06.027.

Shen, S.-z., Crowley, J.L., Wang, Y., Bowring, S.A., Erwin, D.H., Sadler, P.M., Cao, C.-q., Rothman, D.H., Henderson, C.M., Ramezani, J., Zhang, H., Shen, Y., Wang, X.-d., Wang, W., Mu, L., Li, W.-z., Tang, Y.-g., Liu, X.-l., Liu, L.-j., Zeng, Y., Jiang, Y.-f., Jin, Y.-g., 2011. Calibrating the end-Permian mass extinction. Science 334, 1367–1372. http://dx.doi.org/10.1126/science.1213454.

Song, H., Tong, J., Algeo, T.J., Horacek, M., Qiu, H., Song, H., Tian, L., Chen, Z.-Q., 2013a. Large vertical δ^{13}CDIC gradients in Early Triassic seas of the South China craton: implications for oceanographic changes related to Siberian Traps volcanism. Glob. Planet. Change 105, 7–20. http://dx.doi.org/10.1016/j.gloplacha.2012.10.023.

Song, H., Wignall, P.B., Tong, J., Yin, H., 2013b. Two pulses of extinction during the Permian–Triassic crisis. Nat. Geosci. 6, 52–56. http://dx.doi.org/10.1038/ngeo1649.

Sun, Z., Hounslow, M.W., Pei, J., Zhao, L., Tong, J., Ogg, J.G., 2009. Magnetostratigraphy of the Lower Triassic beds from Chaohu (China) and its implications for the Induan–Olenekian stage boundary. Earth Planet. Sci. Lett. 279, 350–361. http://dx.doi.org/10.1016/j.epsl.2009.01.009.

Sun, Y., Joachimski, M.M., Wignall, P.B., Yan, C., Chen, Y., Jiang, H., Wang, L., Lai, X., 2012. Lethally hot temperatures during the Early Triassic greenhouse. Science 338, 366–370. http://dx.doi.org/10.1126/science.1224126.

Sun, Y., Wignall, P.B., Joachimski, M.M., Bond, D.P.G., Grasby, S.E., Sun, S., Yan, C.B., Wang, L.N., Chen, Y.L., Lai, X.L., 2015. High amplitude redox changes in the late Early Triassic of South China and the Smithian–Spathian extinction. Palaeogeogr. Palaeoclimatol. Palaeoecol. 427, 62–78. http://dx.doi.org/10.1016/j.palaeo.2015.03.038.

Szurlies, M., 2004. Magnetostratigraphy: the key to a global correlation of the classic Germanic Trias—case study Volpriehausen Formation (Middle Buntsandstein), Central Germany. Earth Planet. Sci. Lett. 227, 395–410. http://dx.doi.org/10.1016/j.epsl.2004.09.011.

Szurlies, M., 2007. Latest Permian to Middle Triassic cyclo-magnetostratigraphy from the Central European Basin, Germany: implications for the geomagnetic polarity timescale. Earth Planet. Sci. Lett. 261, 602–619. http://dx.doi.org/10.1016/j.epsl.2007.07.018.

Thomson, D.J., 1982. Spectrum estimation and harmonic analysis. Proc. IEEE 70, 1055–1096. http://dx.doi.org/10.1109/PROC.1982.12433.

Tong, J., Zakharov, Y.D., Orchard, M.J., Yin, H.F., Hansen, H.J., 2003. A candidate of the Induan–Olenekian boundary stratotype in the Tethyan region. Sci. China, Ser. D 46, 1182–1200. http://dx.doi.org/10.1360/03yd0295.

Tong, J., Zuo, J., Chen, Z.Q., 2007. Early Triassic carbon isotope excursions from South China: proxies for devastation and restoration of marine ecosystems following the end-Permian mass extinction. Geol. J. 42, 371–389. http://dx.doi.org/10.1002/gj.1084.

Wignall, P., 2015. The Worst of Times: How Life on Earth Survived Eighty Million Years of Extinctions. Princeton University Press.

Wu, H., Zhang, S., Feng, Q., Jiang, G., Li, H., Yang, T., 2012. Milankovitch and sub-Milankovitch cycles of the early Triassic Daye Formation, South China and their geochronological and paleoclimatic implications. Gondwana Res. 22, 748–759. http://dx.doi.org/10.1016/j.gr.2011.12.003.

Wu, H., Zhang, S., Hinnov, L.A., Jiang, G., Feng, Q., Li, H., Yang, T., 2013. Time-calibrated Milankovitch cycles for the late Permian. Nat. Commun. 4, 2452. http://dx.doi.org/10.1038/ncomms3452.

Yang, W., Lehrmann, D.J., 2003. Milankovitch climatic signals in Lower Triassic (Olenekian) peritidal carbonate successions, Nanpanjiang Basin, South China. Palaeogeogr. Palaeoclimatol. Palaeoecol. 201, 283–306. http://dx.doi.org/10.1016/S0031-0182(03)00614-X.

Yin, H.F., Zhang, K.X., Tong, J.N., Yang, Z.Y., Wu, S.B., 2001. The Global Stratotype Section and Point (GSSP) of the Permian–Triassic boundary. Episodes 24, 102–114.

Zhang, K., Lai, X., Tong, J., Jiang, H., 2009. Progresses on study of conodont sequence for the GSSP section at Meishan, Changxing, Zhejiang Province, South China. Acta Palaeontol. Sin. 48, 474–486.

Zhao, L., Orchard, M.J., Tong, J., Sun, Z., Zuo, J., Zhang, S., Yun, A., 2007. Lower Triassic conodont sequence in Chaohu, Anhui Province, China and its global correlation. Palaeogeogr. Palaeoclimatol. Palaeoecol. 252, 24–38. http://dx.doi.org/10.1016/j.palaeo.2006.11.032.

Zhao, L., Chen, Y., Chen, Z.Q., 2013. Uppermost Permian to lower Triassic conodont zonation from Three George area, South China. Palaios 28, 509–522. http://dx.doi.org/10.2110/palo.2012.p12-107r.